



## RESEARCH ARTICLE

# Characteristics of tropical–extratropical cloud bands over tropical and subtropical South America simulated by BAM-1.2 and HadGEM3-GC3.1

Marcia T. Zilli<sup>1</sup>  | Neil C. G. Hart<sup>1</sup> | Caio A. S. Coelho<sup>2</sup> | Robin Chadwick<sup>3,4</sup> |  
Dayana C. de Souza<sup>2</sup> | Paulo Y. Kubota<sup>2</sup>  | Silvio N. Figueroa<sup>2</sup> |  
Iracema F. A. Cavalcanti<sup>2</sup>

<sup>1</sup>School of Geography and the Environment, University of Oxford, Oxford, UK

<sup>2</sup>Center for Weather Forecast and Climatic Studies (CPTEC), National Institute of Space Research (INPE), Cachoeira Paulista, Brazil

<sup>3</sup>Met Office Hadley Centre, Exeter, UK

<sup>4</sup>Global Systems Institute, Department of Mathematics, University of Exeter, Exeter, UK

## Correspondence

Marcia T. Zilli, School of Geography and the Environment, University of Oxford, Oxford, OX1 3QY, UK.

Email: [marcia.zilli@ouce.ox.ac.uk](mailto:marcia.zilli@ouce.ox.ac.uk)

## Funding information

John Fell Fund; Newton Fund - CSSP Brazil; NERC, Grant/Award Number: NE/V011928/1; UKRI Future Leaders Fellowship, Grant/Award Number: MR/W011379/1

## Abstract

Tropical–extratropical cloud bands are common in South America (SAM), contributing significantly to the total rainy season precipitation. Thus, it is fundamental that climate and weather forecast models correctly represent them and their associated dynamic aspects. Adopting an event-based framework, we evaluate the performance of two global models in simulating the observed cloud bands over SAM: the Brazilian Global Atmospheric Model version 1.2 (BAM-1.2) and the Hadley Centre Global Environment Model in the Global Coupled configuration 3.1 (HadGEM3-GC3.1). Both models reproduce the main characteristics of cloud bands and the dynamical aspects leading to their development and persistence. Nonetheless, the biases in precipitation during simulated cloud bands contribute more than 50% of the bias in total precipitation in some regions. BAM-1.2 simulates fewer but more persistent cloud bands than observed; HadGEM3-GC3.1 simulates weaker cloud band activity during early summer and more persistent events after January than observed. In all models, the biases in cloud band events arise from the interaction between biases in the basic state and the synoptic-scale regional circulation. In the basic state, stronger upper level westerlies over the midlatitude South Pacific support the propagation of longer and slower Rossby waves towards subtropical SAM, increasing the duration of the cloud band events. This bias interacts with negative biases in the upper level westerlies over subtropical SAM, increasing the wind shear, hindering the propagation of synoptic-scale Rossby waves into lower latitudes, and resulting in biases in the cloud band location, intensity, and seasonality. The application in this study of an event-based framework robust to differences in model resolution and complexity enables the identification of small but critical biases in circulation. These biases are linked to synoptic-scale rainfall system biases and help to explain the season total rainfall model biases.

## KEYWORDS

circulation bias, climate model evaluation, precipitation bias, rainy season precipitation, South America, tropical–extratropical cloud bands

## 1 | INTRODUCTION

Tropical–extratropical (TE) cloud bands are typical of the subtropical climate, particularly over South America (SAM). Occurring mainly during the rainy season (November–March), they are responsible for more than 60% of the seasonal precipitation over parts of eastern Brazil (EBr; see dotted pink box region in Figure 1; Zilli and Hart, 2021). When present, the cloud bands can produce substantial volumes of precipitation that lead to natural disasters such as landslides and floods. Between 1996 and 2014, at least one natural disaster occurred over southeastern Brazil in 48% of the days characterised as an active South Atlantic convergence zone (SACZ) (da Fonseca Aguiar and Cataldi, 2021), a cloud band that persists four or more days. On the other hand, the absence of cloud bands, especially during the rainy season, is related to droughts, such as the one observed in EBr in 2013–2015 (Coelho *et al.*, 2016a; Coelho *et al.*, 2016b; Cünningham, 2020).

Given their importance to the precipitation climatology over tropical and subtropical SAM, it is fundamental that climate and weather forecast models correctly represent the TE cloud bands and their associated dynamic aspects. Here, we compare the performance of two global models in simulating the observed cloud bands over SAM: the Brazilian Global Atmospheric Model

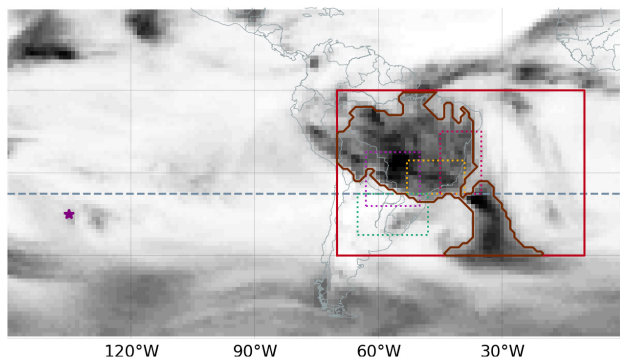


**FIGURE 1** Schematic of the study area: average outgoing long-wave radiation for January 12, 2011 (National Oceanic and Atmospheric Administration Climate Data Record), representing a day with an active South Atlantic convergence zone (shades, low outgoing long-wave radiation values in darker shades), with the region of interest (red square) and the cloud band signature as identified by the algorithm (threshold of  $225 \text{ W} \cdot \text{m}^{-2}$ ; brown contour). The purple star indicates the location of the source of Rossby waves, and the dashed grey line indicates the  $25^\circ \text{ S}$  parallel for the Rossby wave analysis in Figure 8. The dotted rectangles indicate the geographic regions referred to in the text: eastern Brazil (pink), southeastern Brazil (yellow); central South America (purple); and southeastern South America (green) [Colour figure can be viewed at [wileyonlinelibrary.com](https://onlinelibrary.wiley.com)]

version 1.2 (BAM-1.2) and the Hadley Centre Global Environment Model in the Global Coupled configuration 3.1 (HadGEM3-GC3.1). These two models have important climatic and meteorological applications in Brazil. BAM-1.2 is used in the seasonal forecast produced by the Brazilian Center for Weather Forecast and Climatic Studies at the National Institute of Space Research (CPTEC/INPE), whereas the HadGEM3-GC3.1 and its previous generation (HadGEM2-ES) are extensively used as input to regional climate models over the country (Almagro *et al.*, 2020; Dereczynski *et al.*, 2020; Teodoro *et al.*, 2021; Reboita *et al.*, 2022).

Over tropical and subtropical SAM, cloud bands are controlled by the interplay of tropical convection and extratropical transients across different temporal scales (Zilli and Hart, 2021). Over the extratropics, anomalies in the basic-state circulation modulate the equatorward propagation of the synoptic-scale disturbances, modifying the location and persistence of the cloud bands. The mid-latitude disturbances shift the upper level westerly wind towards subtropical latitudes, favouring the development of the persistent cloud band events (Zilli and Hart, 2021), including the SACZ (Kodama, 1992; Kodama, 1993; Carvalho *et al.*, 2011; Gonzalez and Vera, 2014). Over the Tropics, the intensity of the Bolivian high, modulated by convection mainly over the Amazon (Silva Dias *et al.*, 1983; Lenters and Cook, 1997), provides dynamical support to the development of the cloud bands. Transient events (i.e., those lasting up to 3 days) occur when the Bolivian high expands eastward, enhancing the easterlies over subtropical latitudes and shifting the critical line for Rossby wave (RW) propagation further south. In those conditions, mid-latitude disturbances cannot propagate into tropical latitudes and the cloud bands form further south over SAM (Zilli and Hart, 2021). The convection during transient events is fuelled by moisture transported from the Amazon by the low-level jet (LLJ), characteristic of the SACZ inactive phase (Gonzalez and Vera, 2014; Mattingly and Mote, 2017). At the event scale, the anomalous subtropical convection from both persistent and transient cloud bands interacts strongly with the basic flow, resulting in respectively downwind enhancement and damping of the extratropical disturbances (Zilli and Hart, 2021).

Previous studies (García-Franco *et al.*, 2020; Monerie *et al.*, 2020; Coelho *et al.*, 2021) demonstrated that both models reproduce the main characteristics of the seasonal precipitation and circulation over SAM. Coelho *et al.* (2022) further demonstrated the ability of BAM-1.2 and the atmosphere-only version of HadGEM3-GC3.1 in representing the SAM monsoon features, including the Andes LLJ, the upper level Bolivian high, the SACZ, and the lower LLJ level anticyclones over the southeast Pacific and South Atlantic. Both models also reproduce the

dipole-like precipitation pattern between southeastern Brazil and southeastern SAM (see yellow and green box regions respectively in Figure 1) that is associated with synoptic-scale variability in the location of TE cloud bands. However, both models also have biases over SAM. The BAM-1.2 atmosphere is found to be more transparent to long-wave radiation than the observations, which contributes to a misrepresentation of cloud–radiation interactions and leads to an excess of outgoing long-wave radiation (OLR) at the top of the atmosphere (Coelho *et al.*, 2021). This model also overestimates precipitation over the subtropical South Atlantic, extending the simulated dipole-like precipitation pattern in this direction, but it underestimates precipitation over the continent (Coelho *et al.*, 2022). HadGEM3-GC3.1 simulations have atmospheric circulation biases that affect the moisture transport towards southeastern Brazil (see dotted yellow box region in Figure 1), resulting in wet biases over the region (García-Franco *et al.*, 2020; Monerie *et al.*, 2020). These biases generally decrease as the model's horizontal resolution increases (Monerie *et al.*, 2020).

Thus, this article sets out to diagnose the ability of BAM-1.2 and HadGEM3-GC3.1 models to simulate the balance of atmospheric processes described in this section. We present the data in Section 2.1 and methodologies in Sections 2.2 and 2.3, followed by a description of the TE cloud band events identified in both models in Section 3. The circulation aspects simulated by the basic state of each model are described in Section 4, whereas those during the cloud band events identified are described in Section 5. The main biases and related mechanisms are summarised in Section 6, with the final conclusions in Section 7.

## 2 | DATASETS AND METHODOLOGY

### 2.1 | Datasets and model descriptions

#### 2.1.1 | Datasets

We compare the performance of two global climate models in reproducing the characteristics of TE cloud bands identified using satellite imagery. Observed cloud bands are identified using the OLR version 1.2 dataset provided by the National Oceanic and Atmospheric Administration (NOAA) Climate Data Record (CDR; Lee and Program, 2011; Lee, 2014). The observed precipitation and circulation characteristics during cloud band events are drawn from the European Centre for Medium-Range Weather Forecasts fifth-generation reanalysis (ERA5; Hersbach *et al.*, 2020), considering the same period as each model. Previous studies (Balmaceda-Huarte

*et al.*, 2021; Hassler and Lauer, 2021) verified the accuracy of this precipitation product against observational and satellite-based datasets. Zilli and Hart (2021) also corroborated the accuracy of ERA5 daily precipitation during cloud band events when compared with satellite-derived precipitation data (Tropical Rainfall Measuring Mission version 3B42 V7 – TRMM; Huffman *et al.*, 2014), and a gridded dataset based on station-observed precipitation from Brazil (Xavier *et al.*, 2016).

The circulation is characterised by the daily zonal wind  $U$  and meridional wind  $V$  wind at 200 hPa (plus 500 hPa and 850 hPa for BAM-1.2) and the stream function and rotational and divergent wind (at 200 hPa only) computed with the Python package windspharm v1.7.0 (Dawson, 2016), considering spherical harmonics truncated at total wave number 42.

#### 2.1.2 | Model descriptions

BAM-1.2 (Figuroa *et al.*, 2016; Coelho *et al.*, 2021) is an atmospheric spectral model developed by CPTEC/INPE. Adopting a seamless framework, with spatial resolution ranging from  $\sim 10$  to  $\sim 200$  km and time scales ranging from days to seasons, this model is developed for numerical weather forecasts (Figuroa *et al.*, 2016), subseasonal-to-seasonal forecasts (Guimarães *et al.*, 2021), and climate simulations and predictions (Coelho *et al.*, 2021). Here, we consider the same four-member ensemble of the atmosphere-only simulations used in Coelho *et al.* (2021); Coelho *et al.* (2022), covering the 30-year period between 1981 and 2010. The horizontal resolution is  $\sim 100$  km, with a triangular quadratic truncation at 126 waves and 42 sigma vertical levels (TQ0126L042). The initial atmospheric conditions are from the European Centre for Medium-Range Weather Forecasts ERA-40 reanalysis (Uppala *et al.*, 2005), whereas monthly observed sea-surface temperature and sea-ice conditions are from Taylor *et al.* (2000). More information about the model's specifications and experimental design can be found in Coelho *et al.* (2021). The analysis is applied to each ensemble member, and the final values are pooled, resulting in 120 years of data (four members times 30 years each).

HadGEM3-GC3.1 (Williams *et al.*, 2018) is a physical climate model developed by the UK Met Office. Here, we consider two different configurations: atmosphere-only simulations, using prescribed sea-surface temperature and sea ice (Williams *et al.*, 2018; Andrews *et al.*, 2020); and historical simulations with fully coupled atmosphere, ocean, sea ice, and land models (Kuhlbrodt *et al.*, 2018; Williams *et al.*, 2018). Both configurations are analysed at two spatial resolutions: N216 Gaussian grid (HadGEM3-n216; Andrews *et al.*, 2020), which equates

to a nominal atmospheric resolution of  $\sim 60$  km; and N96 (HadGEM3-n96; Kuhlbrodt *et al.*, 2018), with nominal atmospheric resolution of  $\sim 135$  km. For the sake of brevity, we will only show results from the lower resolution (HadGEM3-n96) simulations, but we will comment whenever the results in using higher resolution simulations (HadGEM3-n216) are relevant. These simulations are part of the Coupled Model Intercomparison Project 6. The HadGEM3-GC3.1 simulations considered here cover the period 1979–2014.

## 2.2 | Identification and characterisation of TE cloud band events

Cloud band events are identified through an automated cloud detection algorithm developed by Hart *et al.* (2012); Hart *et al.* (2018a) and adapted to SAM by Zilli and Hart (2021). The algorithm uses a daily mean OLR to identify contiguous areas below a threshold indicative of deep convective cloudiness (see example in Figure 1, shades and brown contour). To be classified as a cloud band, areas of OLR below a selected threshold should diagonally extend from the Tropics to the extratropics within the region of interest (red square in Figure 1). The selected observational threshold for the NOAA CDR OLR dataset is  $225 \text{ W} \cdot \text{m}^{-2}$ , chosen owing to the correspondence between the automatically diagnosed cloud band events and INPE-observer-identified SACZ events (Zilli and Hart, 2021). The selected events are stratified by duration into persistent and transient events. Persistent events last at least 4 days, are more extensive and preferentially located over southeastern and EBr, and have circulation features characteristic of the SACZ. Transient events last up to 3 days and are typically located more poleward than persistent SACZ events. These transient systems tend to have circulation features characteristic of cold fronts. The TE cloud band event-set identified by the automated cloud detection algorithm is described and evaluated by Zilli and Hart (2021).

Before identifying the simulated cloud band events, the daily simulated OLR is regridded to the NOAA CDR OLR grid (with  $1^\circ$  latitude/longitude). In higher spatial resolution datasets, OLR fields are more fragmented, resulting in cloud bands organised as a sequence of smaller features. By regridding it, the small-scale features are smoothed out, resulting in a coherent structure more suitable as input into a feature-tracking algorithm. We use a first-order conservative area-weighted regridding scheme in which each target point is calculated as the weighted mean of all input points intersecting it. The regridding scheme is available through the Python package *iris.analysis* v2.4 (Met Office, 2020).

The regridded simulated OLR is then used to identify the cloud band events. As our objective is to assess the simulated dynamic conditions leading to the organisation of the cloud bands, we calibrate the OLR threshold separately for each dataset to obtain a similar mean monthly frequency of events in all datasets, without affecting the cloud band seasonality. Given the positive model biases in simulated OLR (Monerie *et al.*, 2020; Coelho *et al.*, 2021), using the observational threshold ( $225 \text{ W} \cdot \text{m}^{-2}$ ) would result in an underestimation of the simulated events. Thus, to identify the optimal OLR threshold in each model, we execute the cloud detection algorithm considering thresholds between 210 and  $275 \text{ W} \cdot \text{m}^{-2}$  in steps of  $5 \text{ W} \cdot \text{m}^{-2}$ . For each value, we estimate the average number of days with events and their average persistence per month and compare them with these statistics obtained using observed OLR ( $225 \text{ W} \cdot \text{m}^{-2}$  threshold). The difference between the simulated and observed monthly statistics is averaged over the rainy season (November to March [NDJFM]), resulting in one value for each statistic. These two values are then averaged, and the OLR threshold resulting in the smallest mean difference is chosen as the threshold for that model. The resulting cloud band datasets and their frequency across months and locations allow fair comparison between models and observations. Comparable composites can also be constructed with different datasets because cloud band event sample sizes are roughly equivalent. However, total cloud band numbers across models should not be compared, as these are broadly equivalent by construction.

The simulated OLR thresholds that best represent the observed number of cloud band events and related persistence are  $260 \text{ W} \cdot \text{m}^{-2}$  for BAM-1.2 (all members) and  $245 \text{ W} \cdot \text{m}^{-2}$  for HadGEM3-GC3.1, regardless of the configuration or resolution. These values are larger than the  $225 \text{ W} \cdot \text{m}^{-2}$  threshold adopted for NOAA CDR OLR, but this is expected since all models overestimate the global OLR, especially in equatorial latitudes over land. Over tropical SAM, the bias in BAM-1.2 OLR climatology (compared with the NOAA CDR OLR dataset) during the rainy season is larger than  $+20 \text{ W} \cdot \text{m}^{-2}$  (figure not shown) and similar to the global annual mean bias of  $+17.80 \text{ W} \cdot \text{m}^{-2}$  estimated by Coelho *et al.* (2021). The mean OLR bias in the HadGEM3-GC3.1 simulations is positive over tropical SAM and larger over northeastern Brazil (equatorial Amazon) in the atmosphere-only (fully coupled) configuration. Additionally, the fully coupled simulations have negative OLR biases over the South Atlantic and South Pacific coasts of SAM, with magnitudes below  $-20 \text{ W} \cdot \text{m}^{-2}$ . These biases are related to issues simulating the location of the intertropical convergence zones (ITCZs) and are not present in the atmosphere-only version (figures not shown). Similar OLR biases related to lower level

temperature and precipitation have been described by García-Franco *et al.* (2020).

To compare the characteristics of the cloud band events in each simulation with the observed ones, we compute composites for each day with cloud bands, which are aggregated over all days in each event, before producing monthly averages or totals. This is done at the datasets' native resolutions. For the precipitation-related statistics (total precipitation and contribution to the monthly mean), we only consider values within the spatial signature of the cloud band. The model biases are estimated considering the difference between simulations and observations, with the observations linearly interpolated to the simulation's resolution to avoid penalising coarser resolution models. The significance of the monthly bias is tested using Student's *t*-test for the difference between two means (Wilks, 2011), under the null hypothesis  $H_0$  of indistinctness between them. We also account for the field significance by adjusting the *P*-value (or  $\alpha$  values) to minimise the false discovery rate (Wilks, 2011). Results are estimated monthly but presented as rainy-season averages (NDJFM) for simplicity or as the mean for the onset (November and December [ND]) and core summer (January and February [JF]) seasons when necessary. In those cases, the bias is considered significant when  $H_0$  is rejected in at least three of the five months of the rainy season (NDJFM) or in both months of the onset (ND) and core (JF) seasons.

### 2.3 | Circulation analysis

Zilli and Hart (2021) demonstrated the importance of the basic state in the frequency, location, and persistence of cloud band events. The basic state of the circulation acts as an envelope, modulating the wavelengths and bounding the paths of the synoptic-scale disturbances that result in cloud band events, as explored in Zilli and Hart (2021). Small biases in the simulated upper level circulation can thus affect the characteristics of the midlatitude disturbances and result in cloud band simulation biases. To investigate these biases in the basic-state circulation, we consider the climatology of the zonal and meridional winds ( $\langle U_{200} \rangle$  and  $\langle V_{200} \rangle$  respectively) and zonally asymmetric stream function at 200 hPa ( $\langle ZA\Psi_{200} \rangle$ ), as well as the characteristics of the large-scale RWs supported by the basic state.

As demonstrated by Hoskins and Karoly (1981) and Hoskins and Ambrizzi (1993), the maximum wave number  $-K = (k^2 + l^2)^{1/2}$ , where  $k$  and  $l$  are the zonal and meridional wave numbers respectively – of an RW propagating with zonal phase speed  $c$  is a function of the zonal component of the wind and the meridional gradient of the absolute vorticity  $\beta$ . The trajectories of RWs are estimated

by deriving the dispersion equation for a barotropic RW, resulting in the zonal ( $u_g$ ) and meridional ( $v_g$ ) components of the group velocity (Hoskins and Karoly, 1981; Hoskins and Ambrizzi, 1993):

$$\begin{aligned} u_g &= \frac{\partial \omega}{\partial k} = c_M + \frac{2\beta_M k^2}{K^4}, \\ v_g &= \frac{\partial \omega}{\partial l} = \frac{2\beta_M k l}{K^4}, \end{aligned} \quad (1)$$

where  $\omega$  is the RW frequency,  $k$  and  $l$  are the zonal and meridional wave numbers respectively,  $c_M$  is the zonal phase speed  $c$  in Mercator projection ( $c_M = c / \cos \phi$ , where  $\phi$  is the latitude in radians), and  $\beta_M$  is the meridional gradient of the absolute vorticity in Mercator projection. Full details of estimating the values of  $K$  and  $\beta_M$  are described in Zilli and Hart (2021) and references therein. The trajectory of the RW, as estimated by Equation (1), is not affected by the exact location of the source region but does depend on the spatial variability of the input data ( $\beta_M$  and  $\langle U \rangle$ ). To reduce possible errors due to the different spatial resolutions, we interpolate  $\beta_M$  and  $\langle U \rangle$  to a  $1^\circ$  grid resolution before estimating the trajectories. Equation (1) is then resolved for given values of  $c_M$  and  $k$  using a second-order Runge–Kutta method. These variables are calculated for both observational and simulated values; the calculation is performed using a Python version of the R library package raytracing (Rehbein *et al.*, 2020).

Even though the RW propagation theory is based on a zonally symmetric slow-varying basic state (Hoskins and Karoly, 1981), we consider the local values of  $\langle U \rangle$  and neglect the changes in  $k$  along the ray path, as in Hoskins and Ambrizzi (1993). The assessment of the simulations is based on the comparison of the trajectories of RWs integrated over 15 days, considering the climatology of the monthly zonal wind. This analysis assesses the wave numbers and RW rays supported by the basic state in each simulation.

On synoptic scales, biases in the circulation interact with the RWs as they reach SAM, thus affecting the dynamical aspects of the cloud band events. To investigate this, we adopt the RW source (RWS) framework described in Zilli and Hart (2021). Following Sardeshmukh and Hoskins (1988) and Zilli and Hart (2021),  $RWS = \langle RWS \rangle + RWS'$ , where  $\langle RWS \rangle$  is the basic-state value, calculated as

$$\langle RWS \rangle = -\langle \eta \rangle \langle \nabla \cdot \mathbf{V} \rangle - \langle \mathbf{V}_\chi \rangle \cdot \langle \nabla \eta \rangle, \quad (2)$$

and  $RWS'$  is the synoptic-scale anomaly, calculated as

$$\begin{aligned} RWS' &= -\underbrace{\eta' \langle \nabla \cdot \mathbf{V} \rangle}_{S1.1} - \underbrace{\langle \eta \rangle \nabla \cdot \mathbf{V}'}_{S1.2} \\ &\quad - \underbrace{\langle \mathbf{V}_\chi \rangle \cdot \nabla \eta'}_{S2.1} - \underbrace{\mathbf{V}'_\chi \cdot \langle \nabla \eta \rangle}_{S2.2}. \end{aligned} \quad (3)$$

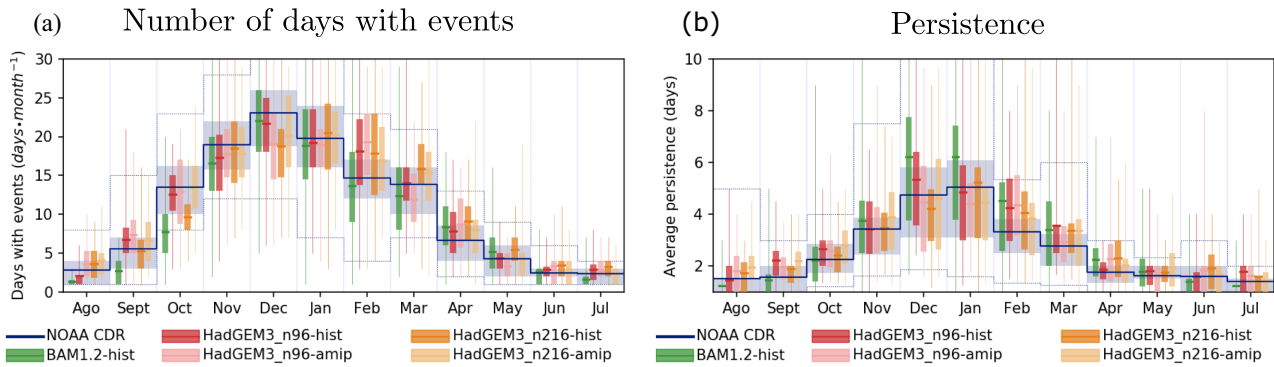


**FIGURE 2** Monthly average, interquartile range, and minimum and maximum values for (a) number of days with cloud band events (in days·month<sup>-1</sup>) and (b) persistence of the events (in days). Simulations (colours in keys at the bottom), represented by the boxplots (monthly average and interquartile range) and whiskers (minimum and maximum values), are compared with values obtained using National Oceanic and Atmospheric Administration Climate Data Record outgoing long-wave radiation, represented by the dark blue line (monthly average), shades (interquartile range), and dotted lines (minimum and maximum values) [Colour figure can be viewed at [wileyonlinelibrary.com](http://wileyonlinelibrary.com)]

In these equations,  $\mathbf{V}$  is the full wind,  $\mathbf{V}_\chi$  is its divergent component, and  $\eta$  is the absolute vorticity. Basic-state values are represented as  $\langle \cdot \rangle$ , whereas synoptic-scale anomalies are indicated by primes. The terms S1.1 and S1.2 represent the components of the RWS' mostly driven by the vortex stretching by the anomalous divergent flow in term S1.2. The terms S2.1 and S2.2 are components of the RWS', dominated by the advection of climatological absolute vorticity by the anomalous divergent wind in term S2.2 (Sardeshmukh and Hoskins, 1988; Qin and Robinson, 1993; Shimizu and Cavalcanti, 2011) which is more typical at lower latitudes. All terms in these equations are estimated using daily data, as proposed in Qin and Robinson (1993); Shimizu and Cavalcanti (2011). The anomalies are calculated for each day of the event and averaged over the event's duration for each dataset.

The statistical treatment of all variables, for both the basic state and the synoptic-scale analysis, is the same as described previously at the end of Section 2.2. For vector fields, the simulations are considered significantly different from the observations when the bias in at least one of its components is statistically significant at the 5% level.

### 3 | REPRESENTATION OF THE TE CLOUD BAND EVENTS

After defining the optimal OLR threshold for each model, we identify the simulated cloud band events. By construction, the total number of days with events and their mean event persistence over the rainy season will be similar between models and observations (Figure 2). However, the calibration of the OLR threshold ensures that the biases in the simulated annual cycle of cloud band frequency are highlighted. BAM-1.2 simulates the main observed

features of the annual cycle of the cloud bands (Figure 2a), although there are too few early-season events in September and October. Also, between December and February, events tend to persist a day longer than in the observations (Figure 2b).

HadGEM3-GC3.1 models better simulate the persistence of the events from October to December but have lower cloud band activity than observations, which shifts the seasonal peak to JF. These biases are larger in the HadGEM3-n96 atmosphere-only simulation (HadGEM3-n96-amip), with four fewer event days in December and 4.6 more event days in February (Figure 2a). These results – a tendency of HadGEM3-GC3.1 simulations to have too many core to late-summer cloud bands than early-season events – are insensitive to the OLR threshold, with adjustments simply moving the event numbers up or down for higher or lower thresholds respectively.

The persistence bias of December–February cloud band events in BAM-1.2 simulations (Figure 2b) increases the total number of cloud band days and is reflected in the wet bias (Figure 3a,c respectively). These events occur preferentially over EBr at the expense of central SAM, where fewer persistent events account for a dry bias (see purple dotted area in Figure 1). These biases over EBr and central SAM account for more than 50% of the total precipitation bias during the rainy season (blue contours in Figure 3e). On the other hand, the number of days with transient events (i.e., those lasting up to 3 days) is reduced (Figure 3b), resulting in a dry bias from these events (Figure 3d) that also contributes to the climatological dry bias over central SAM (red contours in Figure 3e).

The underestimated early-season cloud band activity and overestimation of core summer activity in HadGEM3-GC3.1 simulations show up as distinct biases

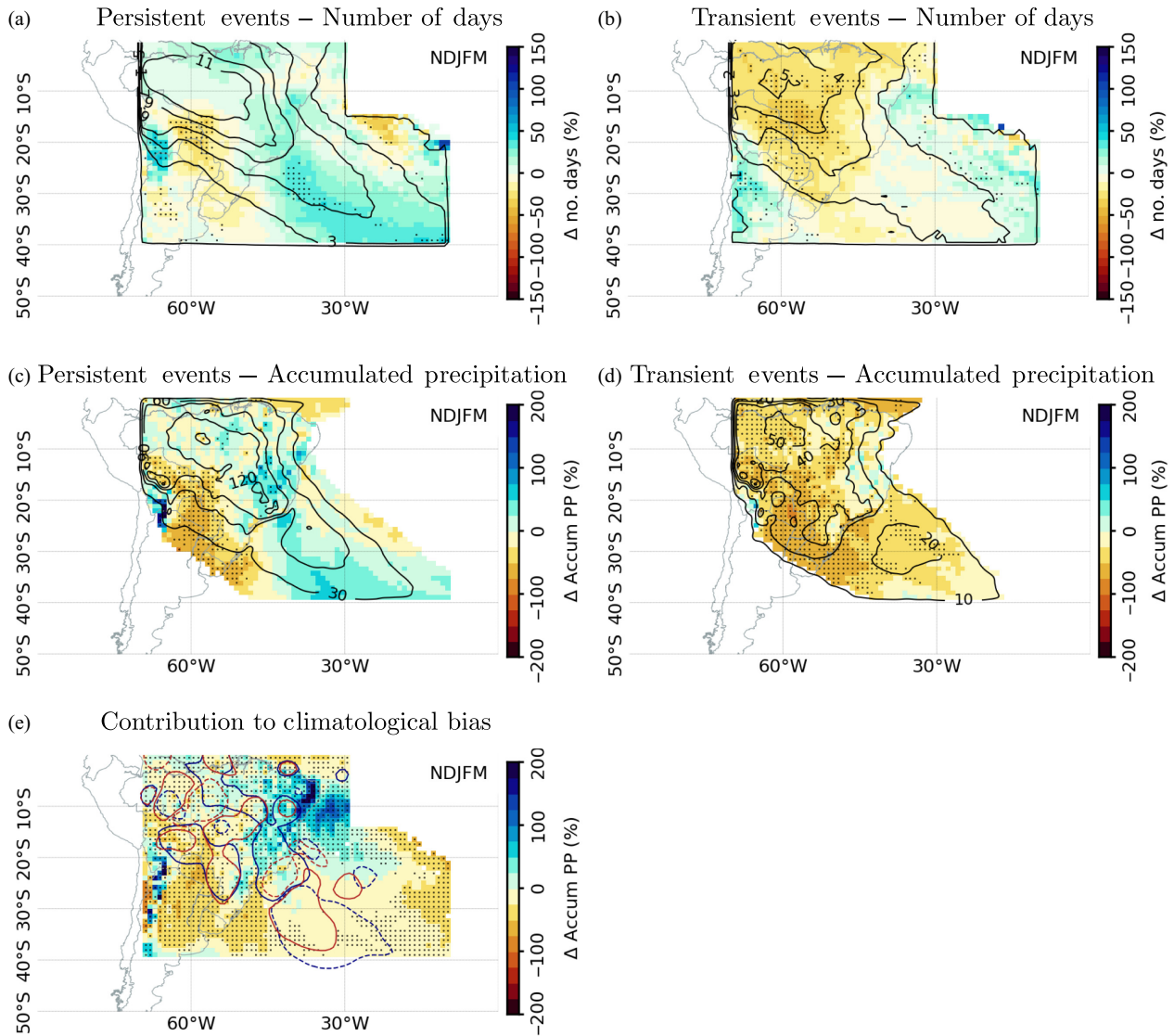


**FIGURE 3** (a)–(d) BAM-1.2 percentage bias (simulations minus observations; shades) and mean observed values (black contours) during (a, c) persistent events and (b, d) transient events averaged over the rainy season. (a, b) Monthly number of days with cloud band events; contours each 2 days-month<sup>-1</sup> (a) and 1 day-month<sup>-1</sup> (b). (c, d) Monthly accumulated precipitation during cloud bands; contours each 30 mm-month<sup>-1</sup> (c) and 10 mm-month<sup>-1</sup> (d). Areas with observed values below 10 mm-month<sup>-1</sup> are masked out. (e) BAM-1.2 percentage bias (simulations minus observations) in the total monthly accumulated precipitation, averaged over the rainy season (shades). Blue (red) contours represent the regions where the bias in simulated precipitation during persistent (transient) events is larger than 50% of the total precipitation bias. Solid (dashed) contours indicate the areas where the simulated bias during cloud band events contributes to (offsets) the total precipitation bias. In all maps, the stippling indicates areas where the bias is statistically significant ( $P < 0.05$ ) in at least three of the five months November to March (NDJFM). Observed events are from National Oceanic and Atmospheric Administration Climate Data Record in (a) and (b) and European Centre for Medium-Range Weather Forecasts fifth-generation reanalysis (ERA5) in (c)–(e). ERA5 values are regridded to the BAM-1.2 resolution before calculating the bias (shades) [Colour figure can be viewed at [wileyonlinelibrary.com](https://onlinelibrary.wiley.com/terms-and-conditions)]

in the spatial distribution of cloud bands during the onset (ND) and core (JF) of the season. As the spatial pattern of the biases is similar during transient and persistent events (figure not shown), we analyse all cloud band events together but consider the onset and core of the cloud band season separately. During ND, all HadGEM3-GC3.1 simulations underestimate the number of days with events over tropical Brazil, resulting in

a dry bias (Figure 4a,b) that accounts for more than 50% of the negative bias in total precipitation over the region (Figure 5a,b). This dry bias is smaller in the fully coupled simulation (HadGEM3-n96-hist; Figure 4b). In JF, the fully coupled simulation shifts the cloud bands northeastward, resulting in more days with cloud band events over EBr and the tropical South Atlantic Ocean and fewer days over the western Amazon and central Brazil (Figure 4f).

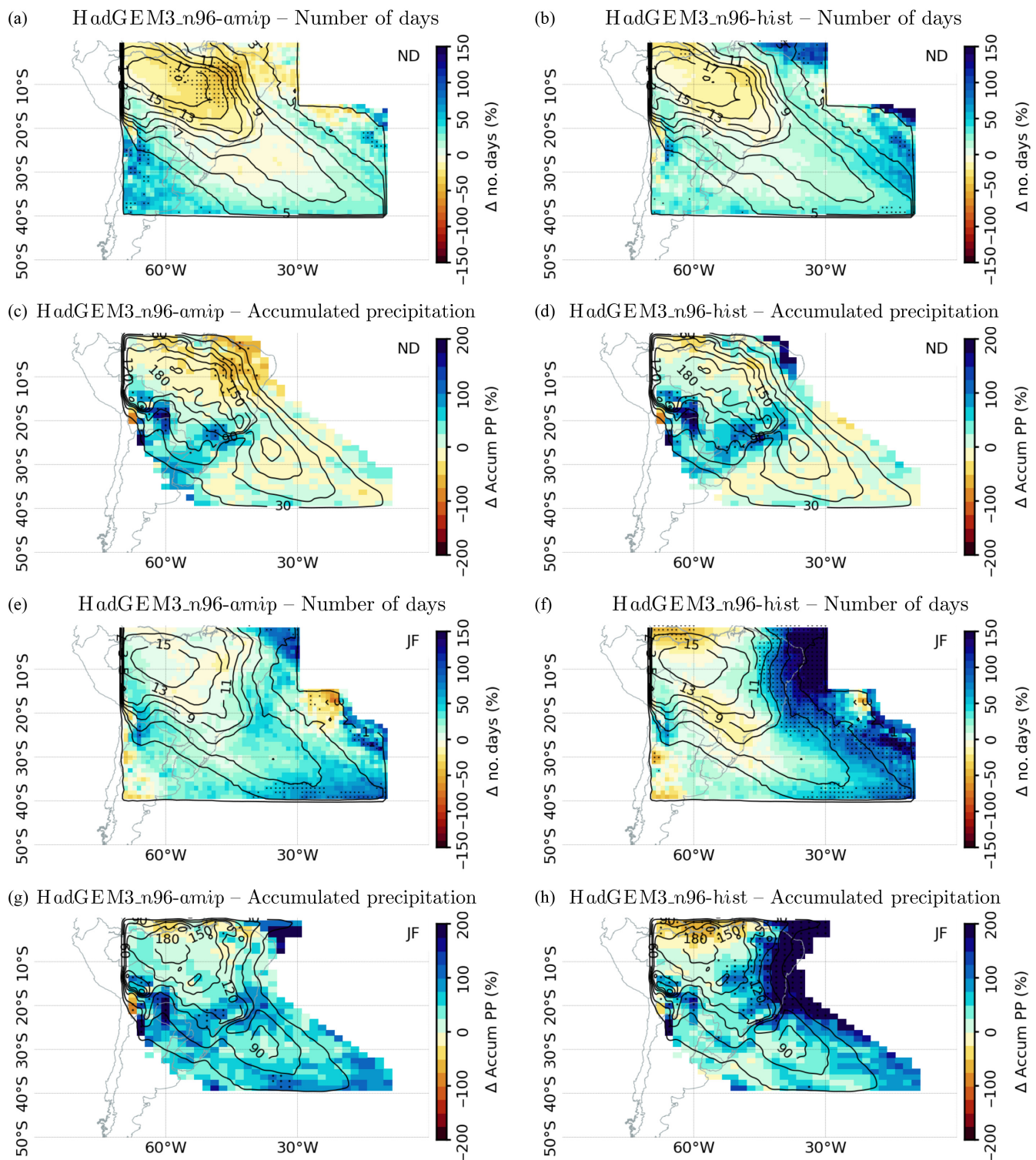


**FIGURE 4** HadGEM3-n96 percentage bias (simulations minus observations; shades) and mean observed values (black contours) for all cloud band events averaged over the (a)–(d) onset (November–December [ND]) and (e)–(h) core (January–February [JF]) of the rainy season, considering atmosphere-only (a, c) and fully coupled (b, d) simulations. Variables are monthly number of days with cloud band events (contours each 2 days·month<sup>-1</sup>) in (a), (b), (e), and (f) and monthly accumulated precipitation during cloud bands (contours each 30 mm·month<sup>-1</sup>) in (c), (d), (g), and (h). Areas with observed values below 10 mm·month<sup>-1</sup> are masked out. In all maps, the stippling indicates areas where the difference is statistically significant ( $P < 0.05$ ) in both months. Observed events are from National Oceanic and Atmospheric Administration Climate Data Record in (a), (b), (e), and (f), and European Centre for Medium-Range Weather Forecasts fifth-generation reanalysis (ERA5) in (c), (d), (g), and (h). ERA5 values are regridded to the HadGEM3-n96 resolution before calculating the bias (shades) [Colour figure can be viewed at [wileyonlinelibrary.com](http://wileyonlinelibrary.com)]



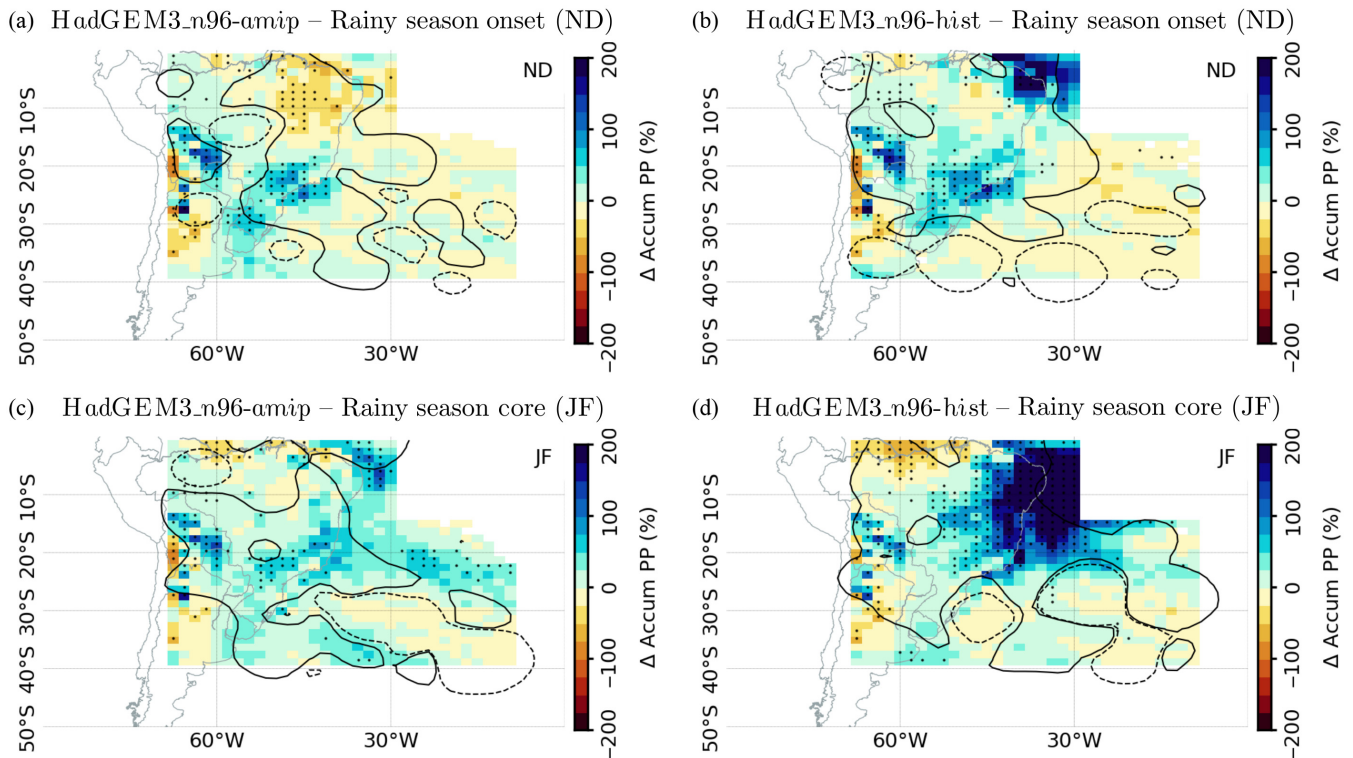


**FIGURE 5** HadGEM3-n96 percentage bias (simulations minus observations; shades) in the total monthly accumulated precipitation averaged over (a), (b) November–December (ND) and (c), (d) January–February (JF), considering atmosphere-only (a, c) and fully coupled (b, d) configurations. The stippling indicates areas where the difference is statistically significant ( $P < 0.05$ ) in both months. Contours represent the regions where the bias in simulated precipitation during cloud band events is larger than 50% of the total precipitation bias, with solid (dashed) contours indicating areas where the bias during cloud band events contributes to (offsets) the total precipitation bias. Precipitation during observed events is from European Centre for Medium-Range Weather Forecasts fifth-generation reanalysis, with values regridded to the HadGEM3-n96 resolution before calculating the bias (shades) [Colour figure can be viewed at [wileyonlinelibrary.com](https://onlinelibrary.wiley.com/doi/10.1002/qj.4470)]

This shift sees cloud bands merge with the ITCZ, resulting in a wet bias over the tropical South Atlantic (Figure 4h) that explains more than 50% of the positive bias in climatological precipitation (blue contours in Figure 5d). Similar biases were also identified in the austral summer (December–February) total precipitation (Kuhlbrodt *et al.*, 2018; García-Franco *et al.*, 2020), with the bias over the ITCZ region reduced in the atmosphere-only simulations due to the use of prescribed sea-surface temperature (García-Franco *et al.*, 2020).

Throughout the rainy season, all HadGEM3-GC3.1 models simulate a wet bias over subtropical SAM (Figure 4c,d,g,h), which contributes to more than 50% of the bias in the total precipitation climatology over the region (Figure 5), especially during the onset of the cloud band season. This wet bias is not caused by the number of days with cloud bands, which are well simulated over the region (Figure 4a,b,e,f), but by a positive bias in precipitation rate (figure not shown). This bias is greater in the higher resolution version of HadGEM3-GC3.1 (n216; figure not shown). Previous studies identified an overestimation of the precipitation rate over subtropical SAM

in HadGEM3-GC3.1 (Kuhlbrodt *et al.*, 2018; Williams *et al.*, 2018; Monerie *et al.*, 2020), associated with stronger lower level northerly winds that advect moisture from the Amazon towards subtropical latitudes (García-Franco *et al.*, 2020).

To summarise, cloud band biases simulated by BAM-1.2 are mainly related to the duration of the events; in HadGEM3-GC3.1 simulations, they arise mainly from the cloud band precipitation rate and seasonality, with different spatial patterns in ND and JF. As demonstrated by Zilli and Hart (2021), the formation and intensity of the cloud bands depend on the interplay between the basic-state flow and the synoptic-scale disturbances during the events, which is now analysed in the next sections.

#### 4 | BASIC-STATE CIRCULATION

The formation of synoptic-scale cloud bands over SAM is modulated by the presence of extratropical disturbances propagating into lower latitudes and interacting with

regional flows. The path and characteristics of this propagation are determined by both the strength of the extratropical eddy-driven jet and the structure and magnitude of the westerly flow across subtropical latitudes (Zilli and Hart, 2021). Over the Tropics, the intensity of the Bolivian high, modulated by convection over the Amazon, locally affects the development of the circulation anomalies during the rainy season (Figuroa *et al.*, 1995; Gandu and Silva Dias, 1998; Nieto-Ferreira *et al.*, 2011). Zilli and Hart (2021) demonstrated that persistent cloud band events are more frequent in the core SACZ location when upper level westerly winds prevail in subtropical latitudes over SAM, supporting the propagation of synoptic-scale RWs towards the Tropics. On the other hand, transient, more poleward, events occur more frequently when the Bolivian high is expanded poleward and eastward, bringing the upper level tropical easterlies into subtropical latitudes.

The models reproduce the main features of the South American upper level circulation represented by the 200 hPa zonal wind  $U_{200}$  (Figure 6a,c,e). However, spatial displacements in key flow structures, such as the midlatitude jet and the Bolivian high, create biases in westerly flow structures as large as 50% locally, which is further shown in the zonally asymmetric stream function  $ZA\Psi_{200}$  (Figure 6b,d,f). This section considers the impact of these basic-state biases on westerly wave propagation and explores the extent to which these flow biases may underpin the cloud band rainfall biases discussed in Section 3.

The anticyclonic anomalies over western SAM are weaker in BAM-1.2 simulations (Figure 6b), as also diagnosed by Coelho *et al.* (2022), and located lower in the troposphere (figure not shown), affecting the dynamical support for the development of synoptic-scale transient cloud bands and reducing their frequency. In HadGEM3-GC3.1 simulations, all configurations shift the Bolivian high southward during ND, but this is improved after January (figures not shown), resulting in its correct placement in the rainy season average (Figure 6d,f). This bias is likely associated with the larger OLR bias and weaker convection over the Amazon (García-Franco *et al.*, 2020) and contributes to the negative bias in the upper level westerlies over subtropical SAM. In the atmosphere-only simulation (HadGEM3-n96-amip), the negative bias in the subtropical westerlies is stronger and extends over the subtropical South Atlantic (Figure 6c), reflecting a midlatitude jet biased a few degrees too far south.

In the extratropics, all models simulate upper level zonal winds (Figure 6a,c,e) that are too strong. This bias is larger in the atmosphere-only HadGEM3-GC3.1 and in BAM-1.2 simulations, in which the midlatitude jet is shifted poleward, also causing a weakening of the westerlies at its equatorward flank and strengthening on the

poleward flank. Coelho *et al.* (2021) identified a similar poleward shift in the midlatitude jet in BAM-1.2 simulations.

To better understand the effects of these biases on midlatitude disturbances, we analyse the trajectory of RWs generated over the subtropical South Pacific ( $135^\circ$  W,  $30^\circ$  S, purple star in Figure 7) as they propagate over the South Pacific Ocean and reach subtropical SAM, disturbing the upper level circulation (see Figure 10). RWs generated over this region are typically forced by the convective activity in the South Pacific convergence zone (SPCZ) and are responsible for most of the barotropic disturbances associated with the occurrence of the SACZ (Grimm and Silva Dias, 1995). In the observed dataset and in all simulations, the SPCZ region has positive and large values of RWS, calculated using Equation (2), during the rainy season (NDJFM; figure not shown), indicating that the basic state of the models allows for RWs to form over the region.

We calculate the trajectory of RWs originating in the SPCZ with zonal wave number  $k = 1-6$  and zonal phase speed  $c < 8 \text{ m}\cdot\text{s}^{-1}$ . The trajectories of four of these RWs are represented in Figure 7, and the longitude at which they cross the  $25^\circ$  S parallel (mean latitude of subtropical SAM) is represented in Figure 8. In ERA5 basic state, RWs with  $k \leq 5$  and  $c \leq 6 \text{ m}\cdot\text{s}^{-1}$  are able to reach the target region between  $60^\circ$  W and  $30^\circ$  W (dark blue diamonds in Figure 8). Longer waves propagate through higher latitudes before turning equatorward and reaching the target region (e.g.,  $k = 2$ , dark blue lines with squares in Figure 7), whereas shorter waves have a more zonal path (e.g.,  $k = 5$ , dark blue lines with upward triangles in Figure 7).

In all simulations, the stronger westerly winds over the South Pacific Ocean increase the meridional wind shear along its equatorward flank, reducing the meridional gradient of absolute vorticity  $\beta_M$  (shades between  $\sim 40^\circ$  S and  $\sim 50^\circ$  S over eastern Pacific in Figure 7). At the entrance of the simulated midlatitude jet (Figure 7), areas of low simulated  $\beta_M$  deflect the RWs with shorter wavelengths ( $k \geq 4$ ) towards the western coast of SAM (e.g.,  $k = 5$ , red and green lines with upward triangles in Figure 7; see also Figure 8). With that, the spectrum of the RWs that can reach the target region is reduced, with only longer and slower RWs (e.g.,  $k = 2$ , red and green lines with squares in Figure 7) reaching subtropical SAM. As a consequence, the support for the development of synoptic-scale events is weakened. On the other hand, the longer and slower RWs that reach the target region produce more persistent cloud band events. This is more evident in BAM-1.2 simulations, in which the bias in the midlatitude zonal wind is larger, restricting the spectrum of the RWs reaching subtropical SAM from the SPCZ to those with  $k \leq 3$  (green symbols in Figure 8). In HadGEM3-GC3.1 simulations, the positive

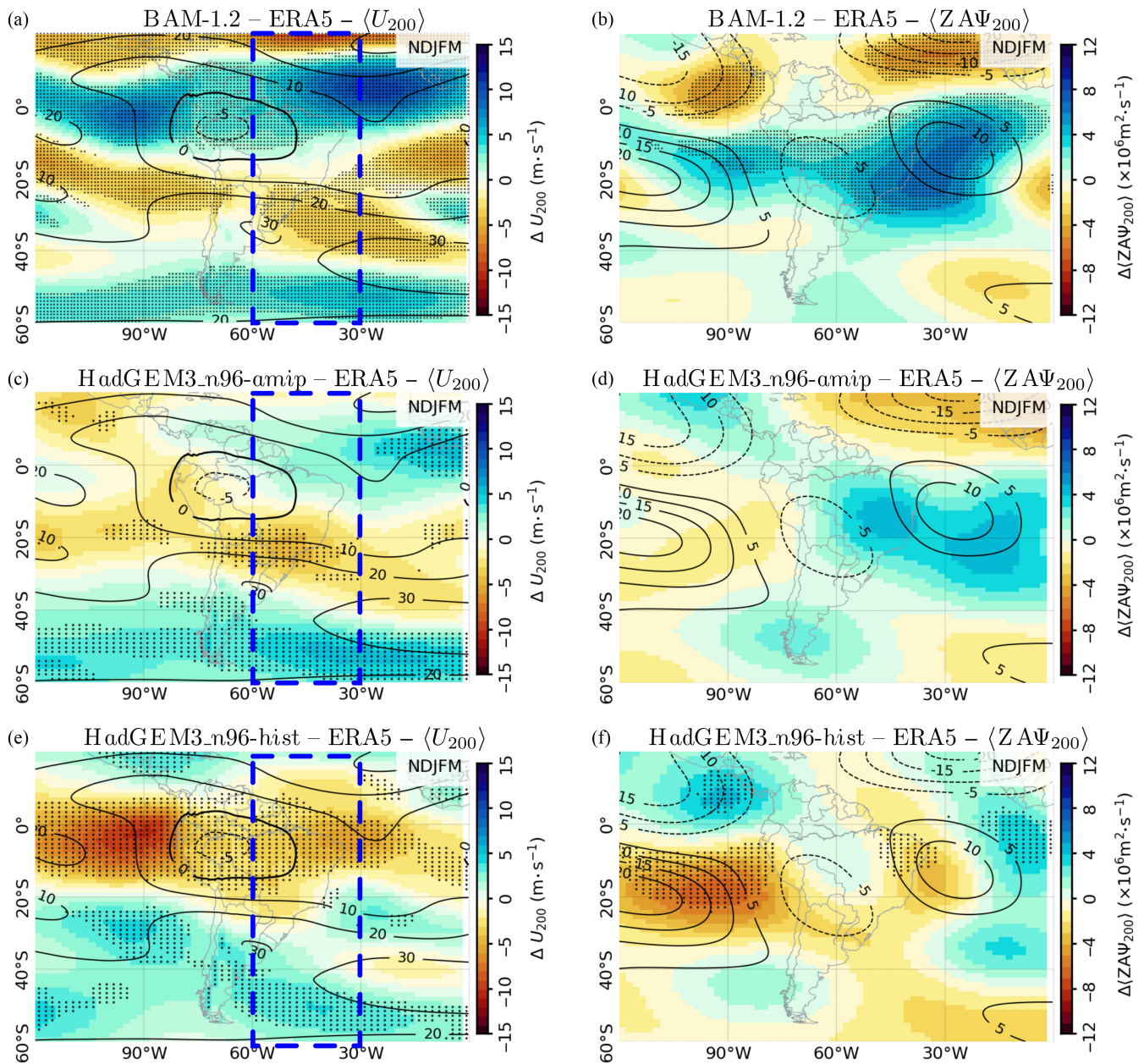


**FIGURE 6** Climatology of European Centre for Medium-Range Weather Forecasts fifth-generation reanalysis (ERA5) zonal wind (left column, black contours each  $10 \text{ m}\cdot\text{s}^{-1}$ , zero bolder and negative dashed) and zonally asymmetric stream function (right column, contours each  $5 \times 10^6 \text{ m}^2 \cdot \text{s}^{-1}$ , zero omitted and negative dashed) at 200 hPa, averaged over the rainy season (November–March [NDJFM]) and the simulations bias (simulations minus observations; shades). (a), (b) BAM-1.2; (c)–(f) HadGEM3-n96 atmosphere-only (c, d) and fully coupled (e, f) simulations. ERA5 averages are regridded to the models' resolutions before calculating the bias (shades). Stippling indicates areas where the model's bias is statistically significant ( $P < 0.05$ ). The dashed blue rectangles (a), (c), and (e) indicate the area over which the latitudinal profiles in Figure 9 are calculated [Colour figure can be viewed at [wileyonlinelibrary.com](https://onlinelibrary.wiley.com)]

bias in the upper level westerlies over subtropical South Pacific is stronger during JF when considering the fully coupled configuration, in which only RWs with zonal wave number  $k < 2$  can reach the target region over subtropical SAM (figures not shown).

As the RWs reach subtropical SAM, the biases in the basic-state circulation affect their propagation over the region. All models simulate weaker zonal winds over

subtropical SAM (Figure 6a,c,e; see also Figure 9a), associated with the poleward shift of the midlatitude jet in BAM-1.2 and the misplacement of the Bolivian high in HadGEM3-GC3.1 simulations. In HadGEM3-GC3.1 simulations, the weakening of the subtropical westerlies is larger between  $20^\circ \text{ S}$  and  $30^\circ \text{ S}$  (Figure 9a) and, combined with the stronger midlatitude westerlies (south of  $40^\circ \text{ S}$ ), increases the extratropical–tropical zonal wind

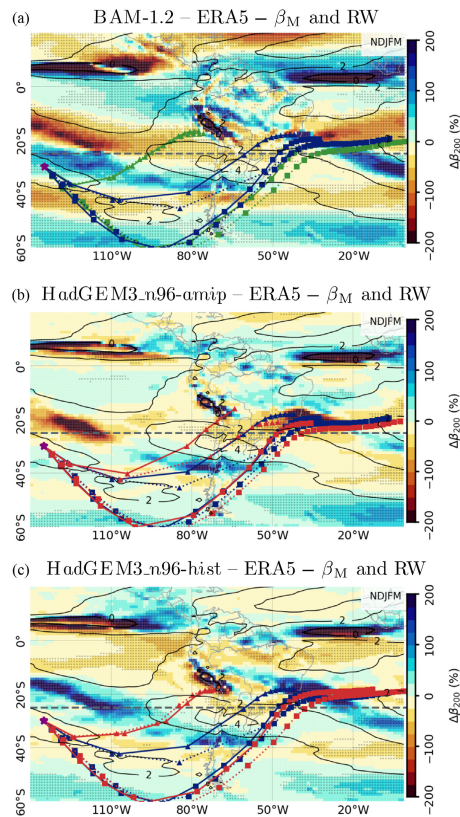


**FIGURE 7** Monthly values of meridional gradient of the absolute vorticity  $\beta_M$  at 200 hPa, averaged over the rainy season (November–March [NDJFM]) considering European Centre for Medium-Range Weather Forecasts fifth-generation reanalysis (ERA5) (black contours each  $2 \times 10^{-11} \text{ m}^{-1} \cdot \text{s}^{-1}$ ) and the model's percentage bias (simulations minus observations; shades). Lines with overlaid symbols represent the trajectories of Rossby waves (RWs) with zonal wave numbers 2 (squares) and 5 (upward triangle) and group velocities of  $4 \text{ m} \cdot \text{s}^{-1}$  (solid line) and  $5 \text{ m} \cdot \text{s}^{-1}$  (dotted lines) generated over the central subtropical South Pacific (purple star at  $135^\circ \text{ W}$ ,  $30^\circ \text{ S}$ ) for ERA5 (dark blue) and (a) BAM-1.2 (green) and (b), (c) HadGEM3-n96 atmosphere-only (b; red) and fully coupled (c; red) simulations. Symbols mark the position of the wave every 12 hr. The dashed line represents the  $25^\circ \text{ S}$  parallel. Datasets are regridded to  $1^\circ$  longitude/latitude resolution before estimating the percentage biases and trajectories [Colour figure can be viewed at [wileyonlinelibrary.com](http://wileyonlinelibrary.com)]

shear, resulting in larger values of  $K$  north of  $\sim 30^\circ \text{ S}$  (Figure 9b). With that, the critical latitude (i.e., the latitude where  $\langle U_M \rangle - c_M = 0$  and  $K \rightarrow \infty$ ) is shifted poleward, obstructing the propagation of RWs into lower latitudes and reducing the number of cloud bands during the onset of the cloud band season in these simulations.

Thus, the biases in the upper level circulation in the basic state affect the characteristics of the midlatitude disturbances in the rainy season. Whereas stronger midlatitude zonal winds favour the propagation of longer RWs towards the region, it also reduces the spectrum of the

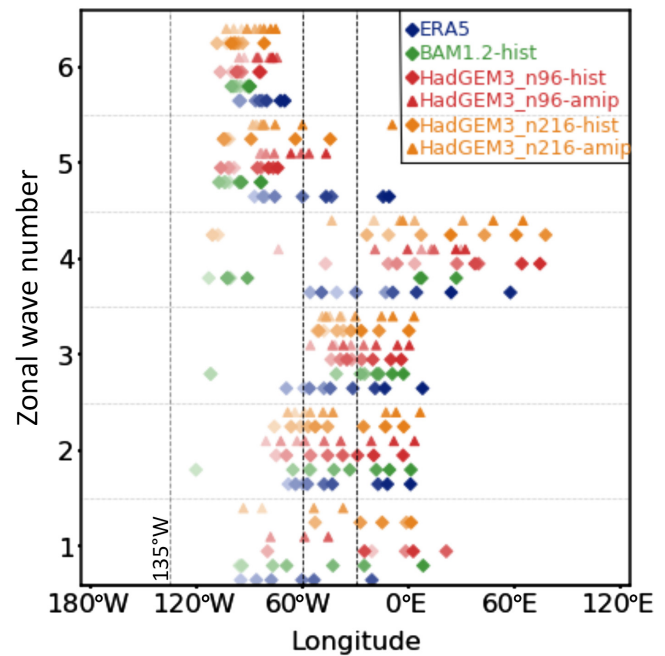


**FIGURE 8** Zonal wave number (y-axis) and longitude (x-axis) at which the Rossby waves sourced over central subtropical South Pacific ( $135^\circ \text{ W}$ ,  $30^\circ \text{ S}$ ; grey dashed line and purple star in Figure 7) cross the  $25^\circ \text{ S}$  parallel (grey dashed line in Figure 7). Slower (faster) group velocities are represented in lighter (darker) shades, varying between  $0 \text{ m} \cdot \text{s}^{-1}$  (stationary Rossby wave) and  $8 \text{ m} \cdot \text{s}^{-1}$ . Values are estimated for the rainy season (November–March [NDJFM]) considering European Centre for Medium-Range Weather Forecasts fifth-generation reanalysis (ERA5; dark blue diamonds) and each model (colour key on the top right). HadGEM3-GC3.1 atmosphere-only (fully coupled) simulations are represented by an upward triangle (diamond) [Colour figure can be viewed at [wileyonlinelibrary.com](http://wileyonlinelibrary.com)]

waves that can reach subtropical SAM, resulting in fewer but longer cloud band events, more evident in BAM-1.2 simulations. Furthermore, the location of the negative bias in westerly winds over subtropical SAM restricts the incursion of the synoptic-scale RWs into lower latitudes, muting the cloud bands' activity during the onset of the season in the HadGEM3-GC3.1 simulations.

## 5 | DYNAMIC CHARACTERISTICS OF THE SIMULATED EVENTS

The biases in the basic state partially explain the issues with the simulated cloud band duration and annual cycle. However, they do not fully address the preferential location of the cloud bands or the precipitation intensity during the simulated events. Thus, we evaluate the models' synoptic-scale circulation during the simulated cloud band events.

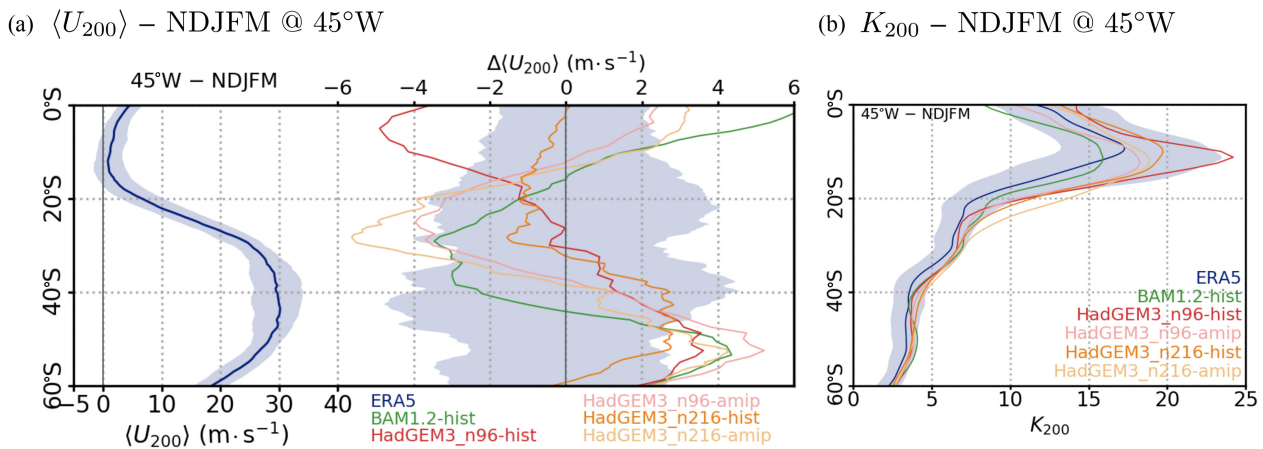


**FIGURE 9** Latitudinal profile of (a) zonal wind (in  $\text{m}\cdot\text{s}^{-1}$ ) and (b) maximum wave number  $K$  for waves with zonal phase speed  $c$  of  $0 \text{ m}\cdot\text{s}^{-1}$  at 200 hPa for each model (colour keys on bottom) compared with European Centre for Medium-Range Weather Forecasts fifth-generation reanalysis (ERA5) values (dark blue lines and shades), averaged over a window of  $\pm 15^\circ$  centred at  $45^\circ \text{W}$  (dashed blue rectangle in Figure 6a,c,e) considering the rainy season (November–March [NDJFM]). Solid blue lines and shades represent the mean and interquartile range respectively for the observed values. In (a), the left curve represents the observed zonal wind climatology; the right curves represent the difference between observations and models (lines) and the interquartile range of the observation centred around its climatological mean (shades). ERA5 values are linearly interpolated to the models' resolutions before estimating the difference [Colour figure can be viewed at [wileyonlinelibrary.com](http://wileyonlinelibrary.com)]

All models correctly reproduce the main circulation characteristics of both persistent and transient events (Figure 10). As described in Zilli and Hart (2021), persistent cloud band events are characterised by upper level (200 hPa) cyclonic anomalies over southern Brazil, part of an RW propagating along the EBr coast (contours in Figure 10a,c,e). The westerly wind anomalies ahead of the cyclonic circulation increase the advection of vorticity over EBr, promoting uplift and supporting convection. Transient cloud band events occur when the upper level circulation anomalies are anticyclonic and centred over South Brazil and the adjacent South Atlantic Ocean (contours in Figure 10b,d,f). During these events, the westerlies are enhanced over midlatitudes, whereas easterly anomalies over the Subtropics obstruct the propagation of the RW into the Tropics.

Despite the good agreement between observed and simulated anomalies, the synoptic-scale stream function anomalies have a meridional orientation (red contours in Figure 10) in contrast with a more zonal orientation observed in ERA5 events (blue contours in Figure 10). In the basic state, the stronger midlatitude westerly winds favour the propagation of longer RWs, with a more meridional path, into subtropical SAM, which matches these synoptic-scale biases. This occurs throughout the rainy season, but in the HadGEM3-GC3.1 simulations they are more evident in JF (see Figure 11e,f). During simulated transient events, the larger meridional component of the RW path results in an anomalous cyclonic circulation centred over the western subtropical South Atlantic ( $\sim 50^\circ$

S,  $\sim 40^\circ \text{W}$ , red contours in Figure 10b,d,f), not present during observed transient events. The orientation of the circulation anomalies affects the pressure gradient and, consequently, the zonal wind anomalies, resulting in the biases represented by the shades in Figure 10.

The bias in the simulated climatological zonal wind (Figure 6a,c,e) also increases the extratropical–tropical anticyclonic meridional shear of the zonal wind. As a result, the upper level cyclonic anomalies during synoptic-scale persistent events are weaker than in the observations and are embedded in a strong anticyclonic environment (contours Figure 10a,c,e), resembling a cut-off low, which may contribute to the longer duration of these events (Figure 2b).

## 5.1 | Wet bias over EBr

All models simulate a wet bias over EBr and southeastern Brazil (pink and yellow region boxes respectively in Figure 1) during persistent events, more prevalent during JF (Figure 11a–c). In BAM-1.2, the simulated cloud bands are narrower, resulting in a wet bias over EBr and a dry bias over central SAM (Figure 11a; see purple region box in Figure 1 for the location of central SAM). In the HadGEM3-GC3.1 fully coupled configuration, the wet bias over the EBr coast extends along the ITCZ (Figure 11c for HadGEM3-n96-hist). Over the ITCZ region, the wet bias is related to larger precipitation rates (figures not shown) and is also present in the

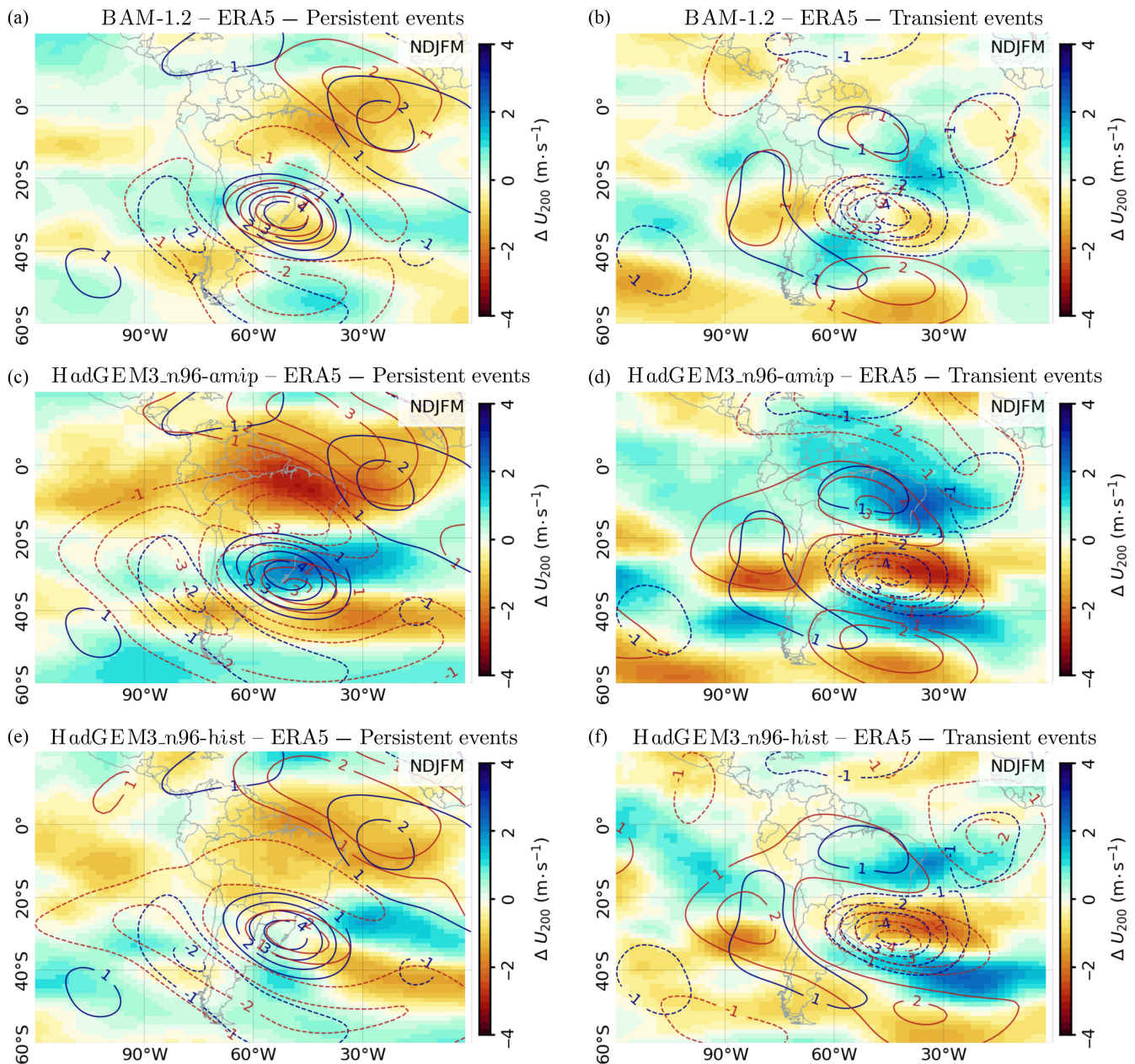


**FIGURE 10** Monthly anomalies of zonally asymmetric stream function (contours each  $1 \times 10^6 \text{ m}^2 \cdot \text{s}^{-1}$ , negative dashed and zero omitted) and the models' biases in zonal wind anomalies (simulations minus observations; shades, in  $\text{m}\cdot\text{s}^{-1}$ ) at 200 hPa averaged over the rainy season (November–March [NDJFM]), considering European Centre for Medium-Range Weather Forecasts fifth-generation reanalysis (ERA5; blue contours) and models (red contours): (a), (b) BAM-1.2 and (c)–(f) HadGEM3-n96 atmosphere-only (c, d) and fully coupled (e, f) simulations. Composites are computed considering persistent (a, c, e) and transient (b, d, f) events. ERA5 anomalies are regridded to the models' resolutions before calculating the bias (shades) [Colour figure can be viewed at [wileyonlinelibrary.com](http://wileyonlinelibrary.com)]

climatology (Kuhlbrodt *et al.*, 2018; Williams *et al.*, 2018; García-Franco *et al.*, 2020).

As mentioned before, the simulated RWs during cloud bands are longer and have a more meridional path, affecting the location of the circulation anomalies (contours in Figure 11d–f) and accelerating the zonal wind anomalies over subtropical SAM and the adjacent subtropical South Atlantic (shades in Figure 11d–f). This bias counteracts

the basic-state easterly anomalies over the region. The stronger wind anomalies also increase the vorticity anomalies, favouring a positive bias in ascending motion and the upper level divergence over EBr and the tropical South Atlantic (figures not shown). The stronger divergence anomalies in HadGEM-GC3.1 enhance the vortex stretching term,  $S_{1.2}$  in Equation (3) (Figure 11g–i), resulting in positive vorticity tendencies (RWS') over the region that

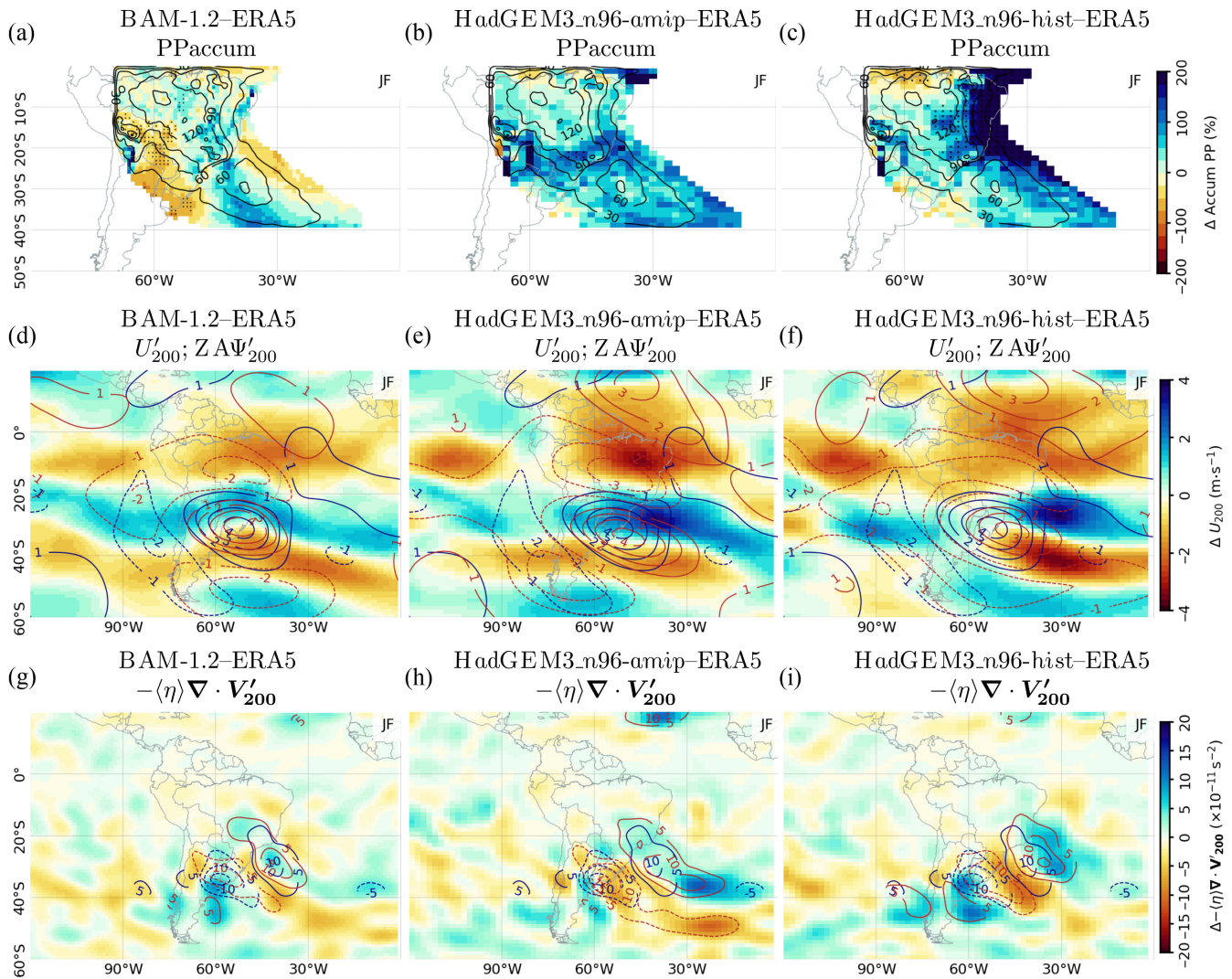


**FIGURE 11** (a)–(c) Mean January–February (JF) accumulated precipitation anomalies in European Centre for Medium-Range Weather Forecasts fifth-generation reanalysis (ERA5; black contours each  $30 \text{ mm} \cdot \text{month}^{-1}$ ; zero omitted) and the models' percentage biases (shades) in (a) BAM-1.2 and (b), (c) HadGEM-n96 atmosphere-only (b) and fully coupled (c) simulations. Areas with observed values below  $10 \text{ mm} \cdot \text{month}^{-1}$  are masked out. (d)–(f) Mean JF circulation anomalies during persistent events at 200 hPa: (d)–(f) zonally asymmetric stream function (contours each  $1 \times 10^6 \text{ m}^2 \cdot \text{s}^{-1}$ ) and the differences (simulations minus observations) in zonal wind (shades); (g)–(i) S1.2 term in Equation (3) (contours each  $5 \times 10^{-11} \text{ s}^{-2}$ ). In (d)–(f), blue contours indicate ERA5 anomalies and red contours BAM-1.2 (a, d, g), HadGEM3-n96 atmosphere-only (b, e, h), and fully coupled (c, f, i) anomalies, with zero contours omitted and negative dashed. Shades indicate the models' biases (percentage bias in a–c). In all maps, the stippling indicates areas where the bias is statistically significant ( $P < 0.05$ ). ERA5 anomalies regridded to the models' resolutions before calculating the bias [Colour figure can be viewed at [wileyonlinelibrary.com](http://wileyonlinelibrary.com)]

favour convection and precipitation along the cloud band (Figure 11a–c). As demonstrated by Zilli and Hart (2021), this term describes most of the vorticity tendency during persistent events.

Additionally, the HadGEM3-GC3.1 fully coupled simulation places the cloud bands northeastward of the observations (Figure 4b,f). Over the subtropical western South Atlantic ( $\sim 30^\circ \text{ W}$ ,  $\sim 25^\circ \text{ S}$ ), the HadGEM3-GC3.1 fully coupled simulation has a positive bias in the basic-state zonal wind throughout the rainy season (Figure 6e), whereas this bias is negative in the atmosphere-only simulation

(Figure 6c). The positive zonal wind bias is stronger during JF and could be associated with a stronger Bolivian high combined with an eastward shift of the Nordeste low in this simulation (figure not shown, but also noticeable in the rainy-season average in Figure 6f). The stronger zonal winds reduce the values of  $K$  over the subtropical western South Atlantic, favouring the propagation of extratropical disturbances towards lower latitudes. During persistent events, this bias is reinforced by stronger westerly wind anomalies on the equatorward flank of the upper level cyclonic anomalies, resulting in a northeastward

shift in the circulation anomalies and cloud band location (Figure 11c,f,i). This northeastward shift occurs only in the fully coupled configuration of the HadGEM3-GC3.1 model, suggesting it could be related to biases in the sea-surface temperature simulations.

## 5.2 | Dry bias over central SAM in BAM-1.2

During both persistent and transient events, BAM-1.2 simulations underestimate the accumulated precipitation, especially over central SAM (Figure 3c,d). This bias occurs throughout the rainy season but is more evident in transient events during ND (Figure 12a). In BAM-1.2, the RW anticyclonic circulation anomalies over South Brazil occur westward of the observed anomalies (Figure 12b), shifting the meridional wind anomalies westward over subtropical SAM and the adjacent South Atlantic (shades Figure 12c). Additionally, the anticyclonic anomalies and associated zonal wind anomalies (figure not shown) are weaker than in ERA5. The biases in the location and intensity of the anticyclonic circulation weaken the upper level vorticity anomalies and their gradient (figures not shown), reducing upper level divergence (Figure 12d). The weaker Bolivian high in this simulation also contributes to the reduction in the upper level divergence. With that, the vorticity tendencies related to vortex stretching – the  $S1.2$  term in Equation (3) – are reduced (Figure 12e). This term drives the negative bias in the vorticity anomalies during transient events (Zilli and Hart, 2021), suggesting a weakening of convection and consequent reduction in the precipitation associated with the transient cloud band events.

This upper level weaker vorticity bias is likely also linked with weaker LLJ transport of moisture southward (at 850 hPa) in BAM-1.2 (Figure 12f). Over central and subtropical SAM, the precipitation during the onset of the rainy season is strongly associated with the location of the LLJ (Salio *et al.*, 2007). When the northerly winds along the tropical Andes are weaker, the flow is predominantly zonal, transporting the Amazonian moisture across central SAM towards the SACZ. On the other hand, episodes of strong northerly winds along the Andes, known as LLJ events, increase the moisture transport towards subtropical SAM, favouring the development of mesoscale convective systems over the region (Mattingly and Mote, 2017; Montini *et al.*, 2019). These anomalies are similar to those observed during transient events (Zilli and Hart, 2021). BAM-1.2 simulates weaker meridional wind anomalies at 850 hPa over central SAM (Figure 12f), reducing the advection of moisture from the Amazon and contributing to the dry biases during ND transient events (Figure 12a), also evident in the rainy-season average (Figure 3d).

## 6 | DISCUSSION

BAM-1.2 and HadGEM3-GC3.1 reproduce the main characteristics of TE cloud bands over SAM as well as the dynamical aspects leading to their development and persistence. Nonetheless, the models have biases in the simulated cloud bands and associated precipitation that contribute to more than 50% of the bias in total precipitation in some regions. Compared with observations, BAM-1.2 simulates fewer transient events but longer persistent events, whereas HadGEM3-GC3.1 models have weaker cloud band activity during early summer and simulate longer persistent events after January. In both cases, the biases in the frequency and seasonality of the cloud bands are caused by the combination of biases in the basic-state upper level flow with those in synoptic-scale circulation anomalies. These biases, as well as the associated mechanisms linking the basic state to the synoptic scale, are represented in Figure 13 and summarised in Figure 14.

Biases in the midlatitude westerly winds in the basic state drive most of the models' shortcomings related to the development of cloud bands and occur throughout the rainy season. Stronger zonal winds over the midlatitude South Pacific (green arrows in Figure 13) support the propagation of longer and slower RWs towards subtropical SAM (red lines in Figure 13), resulting in an increase in the duration of the cloud band events (Figure 14, path no. 1, in green). This mechanism is stronger in BAM-1.2 persistent events and in the atmosphere-only HadGEM3-GC3.1 simulations. Longer waves also have a more meridional path along the eastern SAM coast, inducing biases in the circulation anomalies in synoptic scales (blue arrow and spiral in Figure 13a). The combination of the basic state and the synoptic-scale biases results in stronger convection and precipitation over EBr (Figure 14, path no. 2 in red). These biases occur throughout the rainy season in BAM-1.2 simulations and during JF in HadGEM3-GC3.1 simulations.

In HadGEM3-GC3.1 simulations, the weaker basic-state upper level westerlies over subtropical SAM in ND (green arrow in Figure 13b) affect the wind shear and hinder the propagation of synoptic-scale RWs into lower latitudes (Figure 14, path no. 3 in orange). This bias in the zonal wind is related to biases in the location and intensity of the Bolivian high in these models (brown spiral in Figure 13b) and results in the cloud bands and associated precipitation occurring preferentially over subtropical SAM rather than over EBr (Figure 13b). It is possible that the wet (dry) bias over subtropical SAM (EBr) is enhanced by a stronger LLJ over central SAM (García-Franco *et al.*, 2020; Monerie *et al.*, 2020), which increases the moisture transport from the Amazon into the subtropical region.



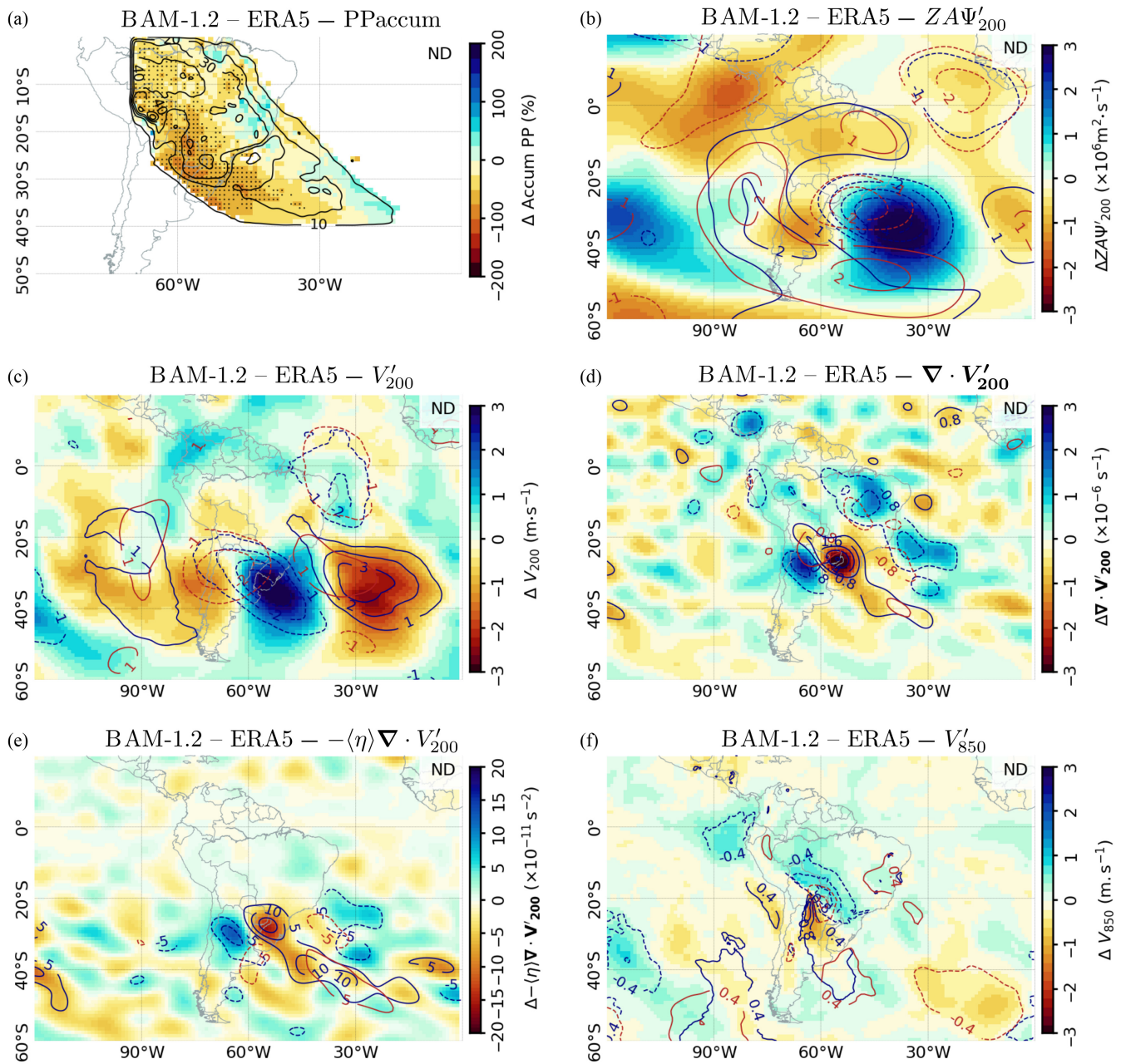
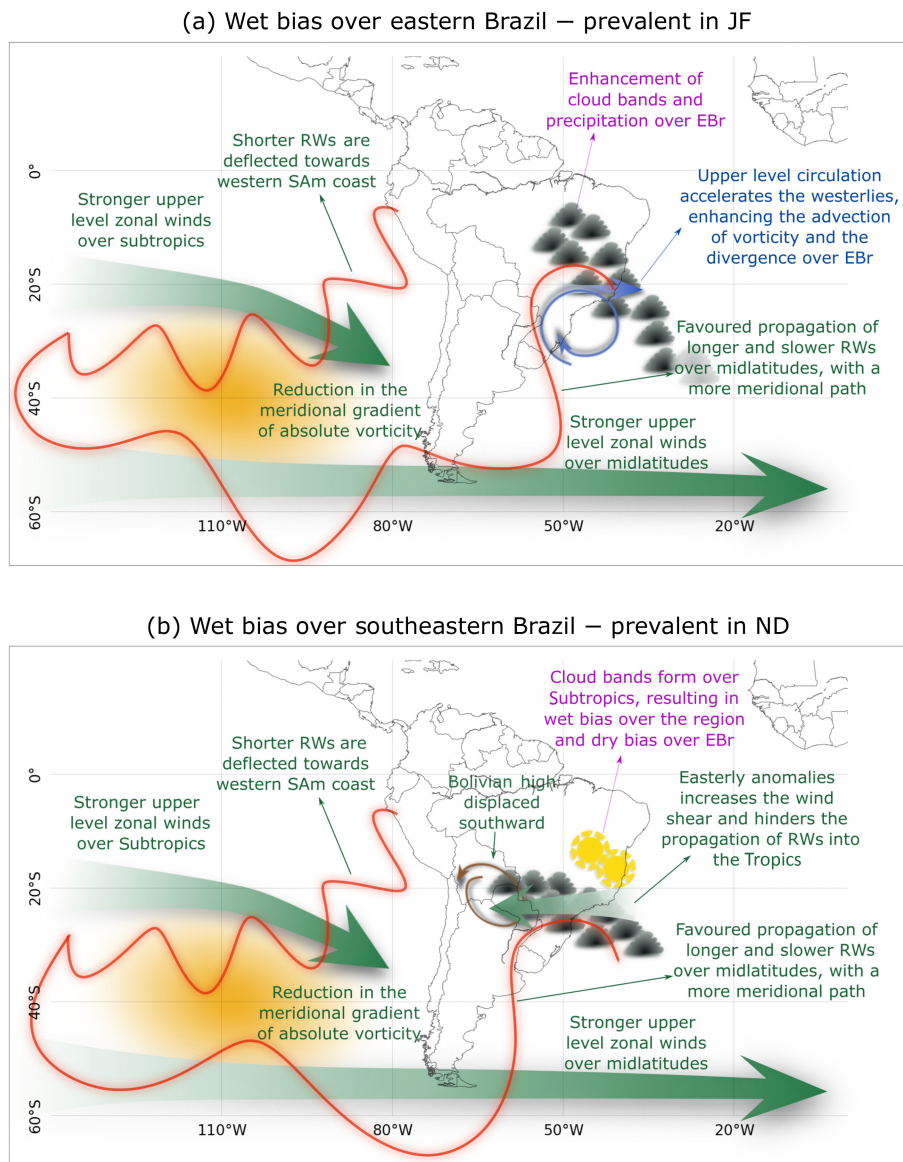


**FIGURE 12** (a) Mean November–December (ND) accumulated precipitation anomalies in European Centre for Medium-Range Weather Forecasts fifth-generation reanalysis (ERA5; black contours each  $10 \text{ mm} \cdot \text{month}^{-1}$ ; zero omitted) and the BAM1.2's percentage bias (shades). Areas with observed values below  $10 \text{ mm} \cdot \text{month}^{-1}$  are masked out. (b)–(f) Mean ND circulation anomalies during transient events: (b) zonally asymmetric stream function at 200 hPa (contours each  $1 \times 10^6 \text{ m}^2 \cdot \text{s}^{-1}$ ); (c) meridional wind at 200 hPa (contours each  $1 \text{ m} \cdot \text{s}^{-1}$ ); (d) divergence at 200 hPa (contours each  $0.8 \times 10^{-6} \text{ s}^{-1}$ ); (e) S1.2 term in Equation (3) (contours each  $5 \times 10^{-11} \text{ s}^{-2}$ ); and (f) meridional wind at 850 hPa (contours each  $0.4 \text{ m} \cdot \text{s}^{-1}$ ). In (b)–(f) the ERA5 (blue contours) and BAM-1.2 (red contours, with zero contours omitted and negatives dashed) anomalies and the model's bias (shades) are shown. In all maps, the stippling indicates areas where the bias is statistically significant ( $P < 0.05$ ). ERA5 anomalies are regridded to BAM-1.2's resolution before calculating the bias [Colour figure can be viewed at [wileyonlinelibrary.com](http://wileyonlinelibrary.com)]

In addition to the previous biases, HadGEM3-GC3.1 fully coupled simulations shift the cloud band events northeastward in JF, reinforcing the wet bias over EBr. In these simulations, the upper level westerly winds over the subtropical South Atlantic are stronger both in the

basic state and during synoptic-scale events, with this bias associated with the location of the upper level circulation anomalies. Together, they favour the propagation of synoptic-scale RWs towards lower latitudes, resulting in the northeastward shift of the cloud band (Figure 14,

**FIGURE 13** Schematic figure representing the main mechanisms associated with the biases in cloud band simulations. (a) Wet bias over eastern Brazil (EBr), prevalent during January–February (JF), and (b) wet bias over southeastern Brazil, prevalent during November–December (ND). Mechanisms related to the basic state are described by the green texts and are similar in both periods. Synoptic-scale mechanisms are described by the blue text and the cloud band events by the pink ones. In both maps, the large green and blue arrows represent the upper level zonal winds; the dark yellow shades indicate the area with biases in the meridional gradient of absolute vorticity; the red lines represent the path of two Rossby waves (RWs). In (a), the brown spiral represents the location of the Bolivian high. In (b), the blue spiral represents the location of the upper level circulation anomalies during persistent events. SAM: South America [Colour figure can be viewed at [wileyonlinelibrary.com](https://onlinelibrary.wiley.com)]



path no. 4 in purple). These simulations also have a wet (dry) bias over northeastern Brazil (equatorial Amazon). Although not discussed here, the wet bias over this region is likely related to the southward displacement of the ITCZ, which weakens the lower level easterlies over the Tropics, increasing the moisture transport from the Amazon into EBr and the precipitation rate in these simulations (García-Franco *et al.*, 2020). The bias related to the location of the ITCZ does not occur in the atmosphere-only simulations, suggesting that they are ultimately caused by biases in the sea-surface temperatures in the fully coupled configurations, as suggested by García-Franco *et al.* (2020).

Finally, BAM-1.2 simulations underestimate the total precipitation and the precipitation rate over central SAM, regardless of the persistence of the event. This model simulates a weaker Bolivian high at upper levels (basic

state) and weaker northerly winds related to the LLJ at lower levels (synoptic scales). The bias in the Bolivian high, caused by the reduced convection mainly over the Amazon, reduces the dynamical support for the development of transient cloud band events (Figure 14, path no. 5a in blue), responsible for a large fraction of the precipitation over central subtropical SAM (Zilli and Hart, 2021). At lower levels, the weakening of the northerly winds reduces the moisture transport from the Amazon towards the region (Figure 14, path no. 5b in blue), reducing the moisture available for convection. These biases explain the dry bias during transient events simulated by BAM-1.2, but they do not fully address the bias in persistent events. Although not explored here, it is possible that the weaker LLJ at a lower level is related to the bias in the intensity of the Bolivian high.

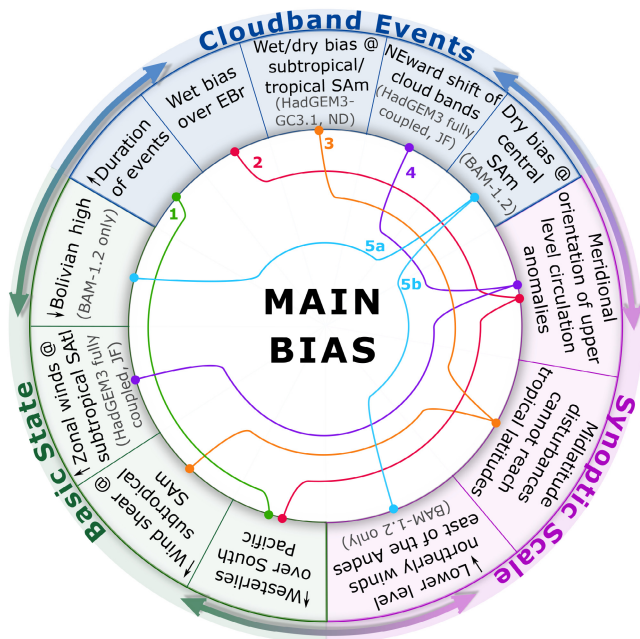


**FIGURE 14** Schematic summarizing the main biases in the models, categorised by biases in the basic state (green shades), synoptic scale (light pink shades), and during cloud band events (blue shades). The paths link the biases across the scales, with the associated mechanisms described in the main text. Biases occur in all models and seasons except when specified. EBr: eastern Brazil; JF: January–February; SAM: South America; SATl: South Atlantic [Colour figure can be viewed at [wileyonlinelibrary.com](https://onlinelibrary.wiley.com)]

The results presented here also highlight circulation biases likely linked to sea-surface temperature bias. The biases in the HadGEM3-GC3.1 atmosphere-only simulations are more similar to those in BAM-1.2, in spite of very distinct dynamical cores and physics packages, than to the fully coupled HadGEM3-GC3.1 configuration. In the atmosphere-only simulations, the upper level zonal wind is shifted poleward over subtropical SAM, a bias that does not occur in the fully coupled simulations. On the other hand, the fully coupled simulations place the ITCZ and associated precipitation southward of its observed location over the tropical Atlantic Ocean, likely linked to sea-surface temperature bias.

Another aspect that should be considered when evaluating BAM-1.2 and HadGEM3-GC3.1 simulations is their spatial geometry and resolution. Despite previous results indicating improvements in biases as the model's horizontal resolution increases (Monerie *et al.*, 2020), the biases during cloud band events obtained using the lower (n96 ~135 km) and medium (n216 ~60 km) HadGEM3-GC3.1 simulations are similar. Nonetheless, it is possible that using convective-permitting simulations could improve the representation of the cloud band events, as observed over southern Africa (Hart *et al.*, 2018a). This hypothesis is the subject of ongoing research. Regarding spatial

geometry, the precipitation bias over the SACZ region is smaller in HadGEM3-GC3.1, which uses a Gaussian latitude–longitude grid (Williams *et al.*, 2018), than in BAM-1.2 simulations, which uses a spectral grid (Coelho *et al.*, 2021). The location and intensity of the precipitation during the SACZ depend on the correct representation of the topography, mainly the Andes to the west of the continent and the coastal mountain ranges over EBr (Figueroa *et al.*, 1995; Lenters and Cook, 1997; Grimm *et al.*, 2007). The decomposition of such steep topography by the spherical harmonics in spectral grids can introduce discontinuities and abrupt shifts, resulting in fictitious oscillations in precipitation, winds, and other atmospheric fields (Navarra *et al.*, 1994). Thus, it is possible that part of the biases related to the intensity of the precipitation along the SACZ in BAM-1.2 simulations is linked to the geometry of the model's grid.

## 7 | CONCLUSIONS

We evaluated one atmosphere-only general circulation model (BAM-1.2) with medium atmospheric resolution (~100 km) and one Earth system model (HadGEM3-GC3.1), considering both its fully coupled and its atmosphere-only configurations, at two different resolutions: ~135 km (n96) and ~60 km (n216). All the model configurations satisfactorily simulate TE cloud band events over SAM despite biases in the events' locations, intensities, and seasonalities. BAM-1.2 simulates fewer but more persistent cloud bands than observed, whereas HadGEM3-GC3.1 simulates weaker cloud band activity during early summer and more persistent events after January than observed. These biases contribute to the biases in simulated seasonal total precipitation. In all models, the issues with the simulated cloud band events arise from the interaction of the biases in the basic-state midlatitude zonal winds at upper levels with those in the synoptic-scale regional circulation. Despite being small, the biases in the basic state are sufficient to affect the structure of the midlatitude synoptic-scale disturbances reaching SAM. The interaction between the biased midlatitude disturbances and the biases in the local flow further intensifies the circulation biases, resulting in biases in TE cloud band location, intensity, and seasonality. Using an event-based dataset to select the main rain-bearing systems facilitates the identification of these small but relevant biases in circulation. Furthermore, this framework is robust to differences in the models' resolutions and complexities. A similar framework was adopted to evaluate regional convective-permitting models over Africa, identifying improvements in the regional circulation that led to a better representation of the cloud band seasonality

over the continent (Hart *et al.*, 2018b). The next steps include applying this framework to identify changes in the SAM cloud band events in convective-permitting simulations and in future scenarios, as well as extending the study area to encompass the entire Southern Hemisphere.

## AUTHOR CONTRIBUTIONS

**Marcia T. Zilli:** conceptualization; data curation; formal analysis; investigation; methodology; software; validation; visualization; writing – original draft; writing – review and editing. **Neil C. G. Hart:** conceptualization; formal analysis; funding acquisition; investigation; methodology; project administration; resources; supervision; validation; visualization; writing – original draft; writing – review and editing. **Caio A. S. Coelho:** conceptualization; data curation; funding acquisition; investigation; methodology; project administration; supervision; validation; visualization; writing – original draft; writing – review and editing. **Robin Chadwick:** conceptualization; formal analysis; methodology; supervision; validation; writing – original draft; writing – review and editing. **Dayana C. de Souza:** conceptualization; data curation; formal analysis; software; validation; visualization; writing – original draft; writing – review and editing. **Paulo Y. Kubota:** conceptualization; data curation; formal analysis; software; validation; visualization; writing – original draft; writing – review and editing. **Silvio N. Figueroa:** conceptualization; formal analysis; supervision; validation; writing – original draft; writing – review and editing. **Iracema F. A. Cavalcanti:** conceptualization; formal analysis; supervision; validation; writing – original draft; writing – review and editing.

## ACKNOWLEDGEMENTS

The Newton Fund supported this work and its contributors through the Met Office Climate Science for Service Partnership Brazil (CSSP Brazil). MTZ and NCGH were also supported with funding from the John Fell Oxford University Press (OUP) Research Fund. NCGH acknowledges support from NERC grant NE/V011928/1 and a UKRI Future Leaders Fellowship MR/W011379/1. CASC thanks Conselho Nacional de Desenvolvimento Científico e Tecnológico (CNPq), process 305206/2019-2, and Fundação de Amparo à Pesquisa do Estado de São Paulo (FAPESP) process 2021/11762-5 for the support received. CASC and IFAC also thank FAPESP process 2015/50687-8 (CLIMAX Project). DCS was supported by CNPq (process 167804/2018-9) and Coordenação de Aperfeiçoamento de Pessoal de Nível Superior (CAPES, process 88887.469114/2019-00).

## ORCID

Marcia T. Zilli  <https://orcid.org/0000-0003-1670-8567>  
Paulo Y. Kubota  <https://orcid.org/0000-0003-4858-1337>

## REFERENCES

- Almagro, A., Oliveira, P.T.S., Rosolem, R., Hagemann, S. and Nobre, C.A. (2020) Performance evaluation of Eta/HadGEM2-ES and Eta/MIROC5 precipitation simulations over Brazil. *Atmospheric Research*, 244, 105053. <https://doi.org/10.1016/j.atmosres.2020.105053>.
- Andrews, M.B., Ridley, J.K., Wood, R.A., Andrews, T., Blockley, E.W., Booth, B., Burke, E., Dittus, A.J., Florek, P., Gray, L.J., Haddad, S., Hardiman, S.C., Hermanson, L., Hodson, D., Hogan, E., Jones, G.S., Knight, J.R., Kuhlbrodt, T., Misios, S., Mizielinski, M.S., Ringer, M.A., Robson, J. and Sutton, R.T. (2020) Historical simulations with HadGEM3-GC3.1 for CMIP6. *Journal of Advances in Modeling Earth Systems*, 12, 1–34. <https://doi.org/10.1029/2019MS001995>.
- Balmaceda-Huarte, R., Olmo, M.E., Bettolli, M.L. and Poggi, M.M. (2021) Evaluation of multiple reanalyses in reproducing the spatio-temporal variability of temperature and precipitation indices over southern South America. *International Journal of Climatology*, 41, 5572–5595. <https://doi.org/10.1002/joc.7142>.
- Carvalho, L.M., Silva, A.E., Jones, C., Liebmann, B., Dias, P.L. and Rocha, H.R. (2011) Moisture transport and intraseasonal variability in the South America monsoon system. *Climate Dynamics*, 36, 1865–1880. <https://doi.org/10.1007/s00382-010-0806-2>.
- Coelho, C.A.S., Cardoso, D.H. and Firpo, M.A. (2016a) Precipitation diagnostics of an exceptionally dry event in São Paulo, Brazil. *Theoretical and Applied Climatology*, 125, 769–784. <https://doi.org/10.1007/s00704-015-1540-9>.
- Coelho, C.A.S., de Oliveira, C.P., Ambrizzi, T., Reboita, M.S., Carpenedo, C.B., Campos, J.L.P.S., Tomaziello, A.C.N., Pampuch, L.A., Custódio, M.D.S., Dutra, L.M.M., Da Rocha, R.P. and Rehbein, A. (2016b) The 2014 southeast Brazil austral summer drought: regional scale mechanisms and teleconnections. *Climate Dynamics*, 46, 3737–3752. <https://doi.org/10.1007/s00382-015-2800-1>.
- Coelho, C.A.S., de Souza, D.C., Kubota, P.Y., Costa, S.M., Menezes, L., Guimarães, B.S., Figueroa, S.N., Bonatti, J.P., Cavalcanti, I.F., Sampaio, G., Klingaman, N.P. and Baker, J.C.A. (2021) Evaluation of climate simulations produced with the Brazilian global atmospheric model version 1.2. *Climate Dynamics*, 56, 873–898. <https://doi.org/10.1007/s00382-020-05508-8>.
- Coelho, C.A.S., Souza, D.C., Kubota, P.Y., Cavalcanti, I.F.A., Baker, J.C.A., Figueroa, S.N., Firpo, M.A.F., Guimarães, B.S., Costa, S.M.S., Gonçalves, L.J.M., Bonatti, J.P., Sampaio, G., Klingaman, N.P., Chevuturi, A. and Andrews, M.B. (2022) Assessing the representation of South American monsoon features in Brazil and U.K. climate model simulations. *Climate Resilience and Sustainability*, 1, e27. <https://doi.org/10.1002/cli.27>.
- Cunningham, C. (2020) Characterization of dry spells in Southeastern Brazil during the monsoon season. *International Journal of Climatology*, 40, 4609–4621. <https://doi.org/10.1002/joc.6478>.
- da Fonseca Aguiar, L. and Cataldi, M. (2021) Social and environmental vulnerability in Southeast Brazil associated with the South Atlantic Convergence Zone. *Natural Hazards*, 109, 2423–2437. <https://doi.org/10.1007/s11069-021-04926-z>.

- Dawson, A. (2016) Windspharm: a high-level library for global wind field computations using spherical harmonics. *Journal of Open Research Software*, 4, 1–5. <https://doi.org/10.5334/jors.129>.
- Dereczynski, C., Chan Chou, S., Lyra, A., Sondermann, M., Regoto, P., Tavares, P., Chagas, D., Gomes, J.L., Rodrigues, D.C. and de los Milagros Skansi, M. (2020) Downscaling of climate extremes over South America—Part I: model evaluation in the reference climate. *Weather and Climate Extremes*, 29, 100273. <https://doi.org/10.1016/j.wace.2020.100273>.
- Figuroa, S.N., Bonatti, J.P., Kubota, P.Y., Grell, G.A., Morrison, H., Barros, S.R., Fernandez, J.P., Ramirez, E., Siqueira, L., Luzia, G., Silva, J., Silva, J.R., Pendharkar, J., Capistrano, V.B., Alvim, D.S., Enoré, D.P., Fábio, L.R., Satyamurti, P., Cavalcanti, I.F., Nobre, P., Barbosa, H.M., Mendes, C.L. and Panetta, J. (2016) The Brazilian global atmospheric model (BAM): performance for tropical rainfall forecasting and sensitivity to convective scheme and horizontal resolution. *Weather and Forecasting*, 31, 1547–1572. <https://doi.org/10.1175/WAF-D-16-0062.1>.
- Figuroa, S.N., Satyamurti, P. and Silva Dias, P.L.D. (1995) Simulations of the summer circulation over the South American region with an Eta coordinate model. *Journal of Atmospheric Sciences*, 52, 1573–1584. [https://doi.org/10.1175/1520-0469\(1995\)052<1573:SOTSCO>2.0.CO;2](https://doi.org/10.1175/1520-0469(1995)052<1573:SOTSCO>2.0.CO;2).
- Gandu, A.W. and Silva Dias, P.L. (1998) Impact of tropical heat sources on the South American tropospheric upper circulation and subsidence. *Journal of Geophysical Research*, 103, 6001–6015. <https://doi.org/10.1029/97JD03114>.
- García-Franco, J.L., Gray, L.J. and Osprey, S. (2020) The American monsoon system in HadGEM3 and UKESM1. *Weather and Climate Dynamics*, 1, 349–371. <https://doi.org/10.5194/wcd-1-349-2020>.
- Gonzalez, P.L.M. and Vera, C. (2014) Summer precipitation variability over South America on long and short intraseasonal timescales. *Climate Dynamics*, 43, 1993–2007. <https://doi.org/10.1007/s00382-013-2023-2>.
- Grimm, A.M., Pal, J.S. and Giorgi, F. (2007) Connection between spring conditions and peak summer monsoon rainfall in South America: role of soil moisture, surface temperature, and topography in eastern Brazil. *Journal of Climate*, 20, 5929–5945. <https://doi.org/10.1175/2007JCLI1684.1>.
- Grimm, A.M. and Silva Dias, P.L. (1995) Analysis of tropical-extratropical interactions with influence functions of a barotropic model. *Journal of the Atmospheric Sciences*, 52, 3538–3555. [https://doi.org/10.1175/1520-0469\(1995\)052<3538:AOTIWI>2.0.CO;2](https://doi.org/10.1175/1520-0469(1995)052<3538:AOTIWI>2.0.CO;2).
- Guimarães, B.S., Coelho, C.A.S., Woolnough, S.J., Kubota, P.Y., Bastarz, C.F., Figuroa, S.N., Bonatti, J.P. and de Souza, D.C. (2021) An inter-comparison performance assessment of a Brazilian global sub-seasonal prediction model against four sub-seasonal to seasonal (S2S) prediction project models. *Climate Dynamics*, 56, 2359–2375. <https://doi.org/10.1007/s00382-020-05589-5>.
- Hart, N.C.G., Reason, C.J.C. and Fauchereau, N. (2012) Building a tropical-extratropical cloud band metbot. *Monthly Weather Review*, 140, 4005–4016. <https://doi.org/10.1175/MWR-D-12-00127.1>.
- Hart, N.C.G., Washington, R. and Reason, C.J.C. (2018a) On the likelihood of tropical-extratropical cloud bands in the south Indian convergence zone during ENSO events. *Journal of Climate*, 31, 2797–2817. <https://doi.org/10.1175/JCLI-D-17-0221.1>.
- Hart, N.C.G., Washington, R. and Stratton, R.A. (2018b) Stronger local overturning in convective-permitting regional climate model improves simulation of the subtropical annual cycle. *Geophysical Research Letters*, 45, 11334–11342. <https://doi.org/10.1029/2018GL079563>.
- Hassler, B. and Lauer, A. (2021) Comparison of reanalysis and observational precipitation datasets including ERA5 and WFDE5. *Atmosphere*, 12, 1462. <https://doi.org/10.3390/atmos12111462>.
- Hersbach, H., Bell, B., Berrisford, P. and Hirahara, S. (2020) The ERA5 global reanalysis. *Quarterly Journal of the Royal Meteorological Society*, 146, 1999–2049. <https://doi.org/10.1002/qj.3803>.
- Hoskins, B.J. and Ambrizzi, T. (1993) Rossby wave propagation on a realistic longitudinally varying flow. *Journal of Atmospheric Sciences*, 50, 1661–1671. [https://doi.org/10.1175/1520-0469\(1993\)050<1661:RWPOAR>2.0.CO;2](https://doi.org/10.1175/1520-0469(1993)050<1661:RWPOAR>2.0.CO;2).
- Hoskins, B.J. and Karoly, D.J. (1981) The steady linear response of a spherical atmosphere to thermal and orographic forcing. *Journal of Atmospheric Sciences*, 38, 1179–1196. [https://doi.org/10.1175/1520-0469\(1981\)038<1179:TSLR0A>2.0.CO;2](https://doi.org/10.1175/1520-0469(1981)038<1179:TSLR0A>2.0.CO;2).
- Huffman, G.J.F.S.E., Bolvin, D.T., Nelkin, E.J. and Adler, R.F. (2014) TRMM (TMPA) rainfall estimate L3 3 hour 0.25 degree x 0.25 degree V7. Accessed 26 September 2016, <https://doi.org/10.5067/TRMM/TMPA/3H/7>.
- Kodama, Y. (1992) Large-scale common features of subtropical precipitation zones (the Baiu frontal zone, the SPCZ, and the SACZ) part i: characteristics of subtropical frontal zones. *Journal of the Meteorological Society of Japan*, 70, 813–836. [https://doi.org/10.2151/jmsj1965.70.4\\_813](https://doi.org/10.2151/jmsj1965.70.4_813).
- Kodama, Y. (1993) Large-scale common features of sub-tropical convergence zones (the Baiu frontal zone, the SPCZ, and the SACZ) part ii: conditions of the circulations for generating the STCZs. *Journal of the Meteorological Society of Japan*, 71, 581–610. [https://doi.org/10.2151/jmsj1965.71.5\\_581](https://doi.org/10.2151/jmsj1965.71.5_581).
- Kuhlbrot, T., Jones, C.G., Sellar, A., Storkey, D., Blockley, E., Stringer, M., Hill, R., Graham, T., Ridley, J., Blaker, A., Calvert, D., Copsey, D., Ellis, R., Hewitt, H., Hyder, P., Ineson, S., Mulcahy, J., Sahaan, A. and Walton, J. (2018) The low-resolution version of HadGEM3 GC3.1: development and evaluation for global climate. *Journal of Advances in Modeling Earth Systems*, 10, 2865–2888. <https://doi.org/10.1029/2018MS001370>.
- Lee, H.-T. (2014) Climate algorithm theoretical basis document (C-ATBD): Outgoing longwave radiation (OLR)—daily. Available at: [https://www1.ncdc.noaa.gov/pub/data/sds/cdr/CDRs/OutgoingLongwaveRadiation-Daily/AlgorithmDescription\\_01B-21.pdf](https://www1.ncdc.noaa.gov/pub/data/sds/cdr/CDRs/OutgoingLongwaveRadiation-Daily/AlgorithmDescription_01B-21.pdf), Accessed 6 November 2019.
- Lee, H.-T. and Program, N.O.A.A.-C.D.R. (2011) NOAA Climate Data Record (CDR) of daily Outgoing Longwave Radiation (OLR), Version 1.2. <https://doi.org/10.7289/V5SJ1HH2>.
- Lenters, J.D. and Cook, K.H. (1997) On the origin of the Bolivian high and related circulation features of the South American climate. *Journal of the Atmospheric Sciences*, 54, 656–677. [https://doi.org/10.1175/1520-0469\(1997\)054<0656:otootb>2.0.co;2](https://doi.org/10.1175/1520-0469(1997)054<0656:otootb>2.0.co;2).
- Mattingly, K.S. and Mote, T.L. (2017) Variability in warm-season atmospheric circulation and precipitation patterns over subtropical South America: relationships between the South Atlantic convergence zone and large-scale organized convection over the La Plata basin. *Climate Dynamics*, 48, 241–263. <https://doi.org/10.1007/s00382-016-3072-0>.

- Met Office. (2020) *Iris: A Python package for analysing and visualising meteorological and oceanographic data sets*. Exeter, Devon, v2.4 edn. Available at <https://scitools-iris.readthedocs.io/en/stable/>.
- Monerie, P.-A., Chevuturi, A., Cook, P., Klingaman, N.P. and Holloway, C.E. (2020) Role of atmospheric horizontal resolution in simulating tropical and subtropical South American precipitation in HadGEM3-GC31. *Geoscientific Model Development*, 13, 4749–4771. <https://doi.org/10.5194/gmd-13-4749-2020>.
- Montini, T.L., Jones, C. and Carvalho, L.M. (2019) The South American low-level jet: a new climatology, variability, and changes. *Journal of Geophysical Research: Atmospheres*, 124, 1200–1218. <https://doi.org/10.1029/2018JD029634>.
- Navarra, A., Stern, W.F. and Miyakoda, K. (1994) Reduction of the gibbs oscillation in spectral model simulations. *Journal of Climate*, 7, 1169–1183. [https://doi.org/10.1175/1520-0442\(1994\)007<1169:ROTGOI>2.0.CO;2](https://doi.org/10.1175/1520-0442(1994)007<1169:ROTGOI>2.0.CO;2).
- Nieto-Ferreira, R., Rickenbach, T.M. and Wright, E.A. (2011) The role of cold fronts in the onset of the monsoon season in the South Atlantic convergence zone. *Quarterly Journal of the Royal Meteorological Society*, 137, 908–922. <https://doi.org/10.1002/qj.810>.
- Qin, J. and Robinson, W.A. (1993) On the Rossby wave source and the steady linear response to tropical forcing. *Journal of Atmospheric Sciences*, 50, 1819–1823. [https://doi.org/10.1175/1520-0469\(1993\)050<1819:OTRWSA>2.0.CO;2](https://doi.org/10.1175/1520-0469(1993)050<1819:OTRWSA>2.0.CO;2).
- Reboita, M.S., Kuki, C.A.C., Marrafon, V.H., de Souza, C.A., Ferreira, G.W.S., Teodoro, T. and Lima, J.W.M. (2022) South America climate change revealed through climate indices projected by GCMs and Eta-RCM ensembles. *Climate Dynamics*, 58, 459–485. <https://doi.org/10.1007/s00382-021-05918-2>.
- Rehbein, A., Ambrizzi, T., Ibarra-Espinosa, S. and Dutra, L.M.M. (2020) Raytracing: An R package for identification and tracking the atmospheric Rossby waves. <https://github.com/salvatorehbein/raytracing>.
- Salio, P., Nicolini, M. and Zipser, E.J. (2007) Mesoscale convective systems over southeastern South America and their relationship with the South American low-level jet. *Monthly Weather Review*, 135, 1290–1309. <https://doi.org/10.1175/MWR3305.1>.
- Sardeshmukh, P.D. and Hoskins, B.J. (1988) The generation of global rotational flow by steady idealized tropical divergence. *Journal of Atmospheric Sciences*, 45, 1228–1251. [https://doi.org/10.1175/1520-0469\(1988\)045<1228:TGOGRF>2.0.CO;2](https://doi.org/10.1175/1520-0469(1988)045<1228:TGOGRF>2.0.CO;2).
- Shimizu, M.H. and Cavalcanti, I.F.A. (2011) Variability patterns of Rossby wave source. *Climate Dynamics*, 37, 441–454. <https://doi.org/10.1007/s00382-010-0841-z>.
- Silva Dias, P.L., Schubert, W.H. and DeMaria, M. (1983) Large-scale response of the tropical atmosphere to transient convection. *Journal of Atmospheric Sciences*, 40, 2689–2707. [https://doi.org/10.1175/1520-0469\(1983\)040<2689:LSROTT>2.0.CO;2](https://doi.org/10.1175/1520-0469(1983)040<2689:LSROTT>2.0.CO;2).
- Taylor, K.E., Williamson, D. and Zwiers, F. (2000) The sea surface temperature and sea ice concentration boundary conditions for AMIP II simulations.
- Teodoro, T.A., Reboita, M.S., Llopart, M., da Rocha, R.P. and Ashfaq, M. (2021) Impacts on the South American monsoon system and its surface-atmosphere processes through RegCM4 CORDEX-CORE projections. *Earth Systems and Environment*, 5, 825–847. <https://doi.org/10.1007/s41748-021-00265-y>.
- Uppala, S.M., Kållberg, P.W., Simmons, A.J., Andrae, U., Bechtold, V.D.C., Fiorino, M., Gibson, J.K., Haseler, J., Hernandez, A., Kelly, G.A., Li, X., Onogi, K., Saarinen, S., Sokka, N., Allan, R.P., Andersson, E., Arpe, K., Balmaseda, M.A., Beljaars, A.C.M., Berg, L.V.D., Bidlot, J., Bormann, N., Caires, S., Chevallier, F., Dethof, A., Dragosavac, M., Fisher, M., Fuentes, M., Hagemann, S., Hólm, E., Hoskins, B.J., Isaksen, I., Janssen, P.A.E.M., Jenne, R., McNally, A.P., Mahfouf, J.-F., Morcrette, J.-J., Rayner, N.A., Saunders, R.W., Simon, P., Sterl, A., Trenberth, K.E., Untch, A., Vasiljevic, D., Viterbo, P. and Woollen, J. (2005) The ERA-40 re-analysis. *Quarterly Journal of the Royal Meteorological Society*, 131, 2961–3012. <https://doi.org/10.1256/qj.04.176>.
- Wilks, D. (2011) Frequentist statistical inference. In: *Statistical methods in the atmospheric sciences*, 3rd edition, Oxford, UK: Academic Press, pp. 133–186. <https://doi.org/10.1016/B978-0-12-385022-5.00005-1>.
- Williams, K.D., Copsey, D., Blockley, E.W., Bodas-Salcedo, A., Calvert, D., Comer, R., Davis, P., Graham, T., Hewitt, H.T., Hill, R., Hyder, P., Ineson, S., Johns, T.C., Keen, A.B., Lee, R.W., Megann, A., Milton, S.F., Rae, J.G.L., Roberts, M.J., Scaife, A.A., Schiemann, R., Storkey, D., Thorpe, L., Watterson, I.G., Walters, D.N., West, A., Wood, R.A., Woollings, T. and Xavier, P.K. (2018) The met office global coupled model 3.0 and 3.1 (GC3.0 and GC3.1) configurations. *Journal of Advances in Modeling Earth Systems*, 10, 357–380. <https://doi.org/10.1002/2017MS001115>.
- Xavier, A.C., King, C.W. and Scanlon, B.R. (2016) Daily gridded meteorological variables in Brazil (1980–2013). *International Journal of Climatology*, 36, 2644–2659. <https://doi.org/10.1002/joc.4518>.
- Zilli, M.T. and Hart, N.C.G. (2021) Rossby wave dynamics over South America explored with automatic tropical-extratropical cloud band identification framework. *Journal of Climate*, 34, 8125–8144. <https://doi.org/10.1175/JCLI-D-21-0020.1>.

**How to cite this article:** Zilli, M.T., Hart, N.C.G., Coelho, C.A.S., Chadwick, R., de Souza, D.C., Kubota, P.Y. *et al.* (2023) Characteristics of tropical–extratropical cloud bands over tropical and subtropical South America simulated by BAM-1.2 and HadGEM3-GC3.1. *Quarterly Journal of the Royal Meteorological Society*, 149(753), 1498–1519. Available from: <https://doi.org/10.1002/qj.4470>